



# Measurement of the Most Important Physics Quantity Ever Discovered

by

Kiyotaka Akabori

Submitted in partial fulfillment of the  
requirements for the degree of  
Doctor of Philosophy

at

Carnegie Mellon University  
Department of Physics  
Pittsburgh, Pennsylvania

Advised by Professor John F. Nagle and Stephanie Tristram-Nagle

June 19, 2014







# Contents

<b>1</b>	<b>Introduction</b>	<b>1</b>
1.1	HIV life cycle . . . . .	1
1.2	Overview of Tat . . . . .	2
<b>2</b>	<b>Materials and Methods</b>	<b>5</b>
2.1	X-ray optics . . . . .	5
2.2	Hydration Chamber . . . . .	5
2.3	Sample Preparation . . . . .	5
2.3.1	Stock Solutions . . . . .	5
2.3.2	Thin Film Samples . . . . .	6
2.4	CCD detector . . . . .	7
<b>3</b>	<b>Structural Perturbation on Lipid Bilayers Due to Tat Peptide</b>	<b>8</b>
3.1	Introduction . . . . .	9
3.2	Materials and Methods . . . . .	12
3.2.1	Volume Measurement . . . . .	12
3.2.2	Analysis of Diffuse Scattering . . . . .	13
3.2.3	Modeling the Bilayer Structure . . . . .	15
3.2.4	Molecular Dynamics Simulation . . . . .	23
3.3	Analysis of Molecular Dynamics Simulation Data . . . . .	24
3.3.1	SIMtoEXP program . . . . .	24
3.3.2	Local Thinning of Membranes . . . . .	24
3.3.3	Lateral Decay Length of Membrane Thinning . . . . .	26
3.4	Results . . . . .	28
3.4.1	Bending and Bulk Modulus . . . . .	28
3.4.2	Volume results . . . . .	28

3.4.3	Electron Density Profile Modeling . . . . .	29
3.4.4	Hard Wall Constraint Fits . . . . .	38
3.4.5	Summary of Electron Density Profile Modeling . . . . .	41
3.4.6	Molecular Dynamics Simulations . . . . .	43
3.5	Discussion . . . . .	51
3.6	Conclusion . . . . .	54
<b>4</b>	<b>Ripple Phase</b>	<b>56</b>
4.1	Introduction . . . . .	56
4.2	Materials and Methods . . . . .	59
4.2.1	Sample Preparation . . . . .	59
4.2.2	Low Angle X-ray Scattering Experiment . . . . .	60
4.2.3	Near Grazing Incidence Wide Angle X-ray Scattering Experiment	62
4.2.4	Transmission Wide Angle X-ray Scattering Experiment . . . . .	65
4.3	Some Theories . . . . .	71
4.3.1	Lattice Structure . . . . .	71
4.3.2	Sample q-space . . . . .	72
4.3.3	Lorentz Correction . . . . .	74
4.3.4	Absorption Correction for LAXS . . . . .	79
4.3.5	Absorption Correction for WAXS . . . . .	81
4.3.6	Effect of mosaic spread . . . . .	81
4.4	Model . . . . .	81
4.4.1	Contour Part of the Form Factor . . . . .	81
4.4.2	Transbilayer Part of the Form Factor . . . . .	82
4.5	Results . . . . .	84
4.5.1	Data and Electron Density Profile . . . . .	84
4.5.2	Near Grazing Incidence Wide Angle X-ray Scattering (NGI- WAXS) . . . . .	84
4.5.3	Transmission WAXS . . . . .	85
4.6	Discussion . . . . .	88
4.7	Conclusion . . . . .	88
	<b>Appendices</b>	<b>89</b>

<b>A</b>	<b>Tat</b>	<b>90</b>
A.1	Analysis of Fixed Angle Data using NFIT . . . . .	90
A.1.1	Theory . . . . .	90
A.1.2	Results . . . . .	90
A.2	Proper Incorporation of Mosaic Spread to NFIT analysis . . . . .	90
A.2.1	Mosaic Spread: Calculation . . . . .	90
A.2.2	Mosaic Spread: Experiment . . . . .	93
A.2.3	Results . . . . .	94
A.3	Domain Size Distribution: Gaussian and Exponential . . . . .	94
A.4	Hard Wall Constraints in SDP . . . . .	94
A.5	Some More Details of Tat Stuff . . . . .	94
<b>B</b>	<b>Ripple Phase</b>	<b>95</b>
B.1	Derivation of the contour part of the form factor . . . . .	95
B.2	Rotation of a Two-Dimensional Function . . . . .	97
B.3	Derivation of the transbilayer part of the form factor in the 2G hybrid model . . . . .	98
B.4	Correction due to refractive index . . . . .	100



# List of Tables

3.1	Some Amino Acids Data . . . . .	12
3.2	DOPC basic structural parameters. $n_i^e$ and $\rho_i$ are the number of electrons and average electron density per component, respectively. . . .	20
3.3	DOPE basic structural parameters. The notations are the same as in Table 3.2. . . . .	20
3.4	DOPC:DOPE (3:1) basic structural parameters. The notations are the same as in Table 3.2. . . . .	20
3.5	Tat basic structural parameters. The notations are the same as in Table 3.2. . . . .	21
3.6	Volumetric constraints. A and B refer to two different models described in the text. . . . .	21
3.7	Important Quantities for Tat Peptide . . . . .	29
3.8	Measured Quantities in . . . . .	29
3.9	Fitting Results for DOPC membranes for the THG model. $\Delta z_1 = z_{PC} - z_{CG}$ and $\Delta z_2 = z_{CG} - z_{HC}$ . . . . .	32
3.10	Fitting Results for DOPC:DOPE (3:1) membranes for the THG model. $\Delta z_1 = z_{PC} - z_{CG}$ and $\Delta z_2 = z_{CG} - z_{HC}$ . . . . .	33
3.11	Fitting Results for DOPC:DOPE (1:1) membranes for the THG model. $\Delta z_1 = z_{PC} - z_{CG}$ and $\Delta z_2 = z_{CG} - z_{HC}$ . (Need to work) . . . . .	36
3.12	Fitting Results of the bound THG model for DOPC membranes. $\Delta z_1 = z_{PC} - z_{CG}$ and $\Delta z_2 = z_{CG} - z_{HC}$ . . . . .	39
3.13	Comparison of the simulated form factors to the experimental form factors. . . . .	48

3.14	Summary of simulation results. $\langle D_{\text{PP}} \rangle$ , phosphorus-phosphorus distance averaged over all lipids; $D_{\text{PP}}$ , Tat-perturbed phosphorus atoms; $x$ , thickness away from Tat; $\Delta t$ , $\langle D_{\text{PP}}^{\text{DOPC}} \rangle - D_{\text{PP}}$ ; $H_{\text{Tat}}$ , Tat height; $R_{\text{Tat}}$ , radius of Tat cylinder; $R_2$ , radius of the calculated in-plane Tat-perturbed region; $R_3$ , effective radius of the simulation box. . . . .	49
3.15	Summary of weighted average results. The caption is the same as Table 3.14. . . . .	49
4.1	Lattice constants for DMPC at $T = 18.0$ °C reported by Wack and Webb [1]. . . . .	58
4.2	Definitions of $Z_{\text{CH}_2}$ and $Z_{\text{W}}$ . . . . .	83
4.3	Lattice constants . . . . .	84

# List of Figures

3.1	Schematic of DOPC showing each lipid component. The dash lines show where the lipid is divided into different components. The lipid headgroup is divided into two components, phosphate-choline and carbonyl-glycerol. The hydrocarbon chain region is also divided into two components, methylene+methine and terminal methyl groups. . . . .	16
3.2	A model electron density profile for DOPC with Tat. . . . .	17
3.3	test . . . . .	25
3.4	test . . . . .	26
3.5	The best fits to DOPC form factors (left) and the corresponding electron density profiles (right) with $x_{\text{Tat}} = 0, 0.016, 0.034,$ and $0.059$ (from top to bottom). . . . .	31
3.6	The best fits to DOPC:DOPE (3:1) form factors (left) and the corresponding electron density profiles (right) with $x_{\text{Tat}} = 0, 0.016, 0.034,$ and $0.059$ (from top to bottom). . . . .	34
3.7	The best fits to DOPC:DOPE (1:1) form factors (left) and the corresponding electron density profiles (right) with $x_{\text{Tat}} = 0, 0.016, 0.034,$ and $0.059$ (from top to bottom). . . . .	35
3.8	$\chi^2$ as a function of $z_{\text{Tat}}$ for DOPC, DOPC:DOPE (3:1), and DOPC:DOPE (1:1) (from left to right) with $x_{\text{Tat}} = 0.016, 0.034,$ and $0.059$ (from top to bottom). $\sigma_{\text{Tat}} = 3.0$ . The THG model (black squares) and the THC model (red circles). . . . .	37
3.9	$\chi^2$ as a function of $z_{\text{Tat}}$ for DOPC with $x_{\text{Tat}} = 0.016, 0.034,$ and $0.059$ (from top to bottom). $\sigma_{\text{Tat}} = 3.0$ . The bound THG model was used. .	40
3.10	DPP graph . . . . .	41
3.11	DHH graph . . . . .	41
3.12	AL graph . . . . .	41

3.13	$z_{\text{Tat}}$ graph . . . . .	42
3.14	MD simulated form factors for DOPC at $A_L = 68 \text{ \AA}^2$ (blue solid line), 70 $\text{\AA}^2$ (red solid line), and 72 $\text{\AA}^2$ (green solid line) compared to the experimental form factor (open circles) scaled vertically to best match the form factor for 70 $\text{\AA}^2$ . . . . .	44
3.15	The simulated, symmetrized electron density profile for DOPC at $A_L =$ 70 $\text{\AA}^2$ as a function of the distance away from the bilayer center. Each component profile is labeled with its name: PC (phosphate-choline), CG (carbonyl-glycerol), $\text{CH}_2+\text{CH}$ (methylene-methine combination), $\text{CH}_3$ (terminal methyl). The sum of all the components is labeled as total. . . . .	45
3.16	MD simulated form factors for DOPC with $x_{\text{Tat}} = 0.015$ at $A_L =$ 72 $\text{\AA}^2$ (top) and 74 $\text{\AA}^2$ (bottom), with $z_{\text{Tat}} = 18 \text{ \AA}$ (red solid lines), 16 $\text{\AA}$ (green solid lines), and 14 $\text{\AA}$ (blue solid lines) compared to the experimental form factor (open circles) scaled vertically to best match the form factor for $z_{\text{Tat}} = 18 \text{ \AA}$ . . . . .	46
3.17	MD simulated form factors for DOPC with $x_{\text{Tat}} = 0.030$ at $A_L =$ 74 $\text{\AA}^2$ (top) and 76 $\text{\AA}^2$ (bottom), with $z_{\text{Tat}} = 18 \text{ \AA}$ (red solid lines), 16 $\text{\AA}$ (green solid lines), and 14 $\text{\AA}$ (blue solid lines) compared to the experimental form factor (open circles) scaled vertically to best match the form factor for $z_{\text{Tat}} = 18 \text{ \AA}$ . . . . .	47
3.18	Electron density profiles of guanidinium groups from the four best matched simulations for DOPC with $x_{\text{Tat}} = 0.015$ (one Tat on each leaflet). Tat on the lower and upper leaflets are shown on the left and right plots, respectively. . . . .	50
4.1	Lattice structure of the DMPC ripple phase. Unit cells are shown in dash lines. Center of bilayers are shown by thick, solid lines. Notations in the figure are <b>a</b> and <b>b</b> : lattice unit vectors, $D$ : $D$ -spacing along $z$ , $D_s$ : stacking distance, $\lambda_r$ : ripple wavelength, $\gamma$ : oblique tilt angle, $A$ : ripple amplitude, and $x_0$ : projected length of the major arm. . . . .	57
4.2	A picture of an annealing chamber. Need to take a picture . . . . .	59
4.3	The horizontal profile of the beam used in the low resolution study. . .	60
4.4	The vertical profile of the beam used in the low resolution study. . . .	61

4.5	1 second exposure (left) and 60 second exposure (right) of the low angle X-ray scattering from the DMPC ripple phase. The dark rectangle in the right image extending from $q_z = 0 \text{ \AA}^{-1}$ to $0.2 \text{ \AA}^{-1}$ is the shadow cast by $100 \text{ }\mu\text{m}$ thick molybdenum beam stop. $D = 57.8 \text{ \AA}$ , $\lambda_r = 145.0 \text{ \AA}$ , and $\gamma = 97.8^\circ$ . The gray scales used are $[0 \ 100]$ (left) and $[0 \ 500]$ (right). . . . .	63
4.6	CCD images of X-ray scattering taken with (left) and without (right) a nominally $25 \text{ }\mu\text{m}$ thick Mo attenuator. These data were taken at a fixed angle of incidence. The sample was an oriented film of DOPC:DOPE (3:1) in the fluid phase at $37^\circ\text{C}$ . The wavelength was $1.175 \text{ \AA}$ , the same as the one used for the ripple phase experiment. The same gray scale is used in both images. . . . .	64
4.7	Vertical $p_z$ slices of X-ray images shown in Fig. 4.6 (left). The scattering intensity measured with the attenuator (red solid circles) was multiplied by a factor of 6.9 and compared to the intensity measured without the attenuator (black solid circles, right). . . . .	64
4.8	Beam used in the high resolution experiment. The horizontal beam profile (left) and vertical beam profile (right) are shown. . . . .	66
4.9	The geometric broadening due to the sample width and the beam width. A top view of the sample (gray), Si wafer (blue), and incoming and diffracted X-rays (bounded by red solid lines) are shown. The horizontal beam width is labelled as $\Delta x_{\text{beam}}$ , the sample width as $w_s$ , the total scattering angle for a lipid chain-chain correlation as $2\theta$ , and the geometric broadening as $\Delta x$ . . . . .	66
4.10	Schematics of the sample holder showing a small piece I fabricated . .	67
4.11	Picture of the sample holder looking from the above. A lead tape was attached to the back of the sample holder to help reduce the background scattering, typically coming from the air gap between the flightpath snout and the mylar window of the chamber. . . . .	68
4.12	Schematics of the sample holder in the transmission mode. . . . .	68
4.13	Sample holder geometry. . . . .	68
4.14	Geometric broadening in TWAXS. The cross section of the incoming X-ray with the sample and the CCD detector are both shaded in red. . . . .	69

4.15	Top view of geometric broadening in TWAXS. The cross section of the incoming X-ray with the sample is shaded in red. . . . .	69
4.16	Side view of geometric broadening in TWAXS. The cross section of the outgoing X-ray with the CCD detector is shaded in red. . . . .	70
4.17	Projection of rectangular beam on the detector. . . . .	70
4.18	Experimental reflectivity geometry. . . . .	73
4.19	Ewald sphere construction for the ripple phase diffraction in the low angle regime. A ripple $k = 0$ peak is the solid, black circle on the $q_z$ -axis. A ripple $k \neq 0$ ring is the black ring centered about the $q_z$ -axis. The portion of the ring that is inside the Ewald sphere is shown as a red dashed line and the portion of the ring that is outside but behind the Ewald sphere is shown as a black dotted line. The magnitude of the total scattering angle is exaggerated. With a wavelength of $1.175 \text{ \AA}$ , the magnitude $ \mathbf{k}_{\text{in}}  = 5.35 \text{ \AA}^{-1}$ . For a $h = 5$ peak, $q_{50}^z = 0.54 \text{ \AA}^{-1}$ , one tenth of $k_{\text{in}}$ . . . . .	76
4.20	Side view of an arc of $k = 0$ peak shown as a light blue line. . . . .	77
4.21	$q$ -space representations of Bragg peaks and Bragg rings for $h = 1$ and $k = 0, 1$ , and $2$ in $q_{hk}^z$ planes. The shaded rectangles show cross sections of the rotating Ewald sphere along $q_{hk}^z$ plane. The intersection between the Ewald sphere and a Bragg peak/ring is indicated in red. The observed intensity for the $k \neq 0$ orders is proportional to the fraction of the length of red arcs in the circumference. This fraction is equal to one for a $k = 0$ order. Because the orders are not in the same $q_z$ plane, the range of $q_y$ integration indicated by the height of the rectangle is different for different orders. The magnitude of curvature of arcs is exaggerated. . . . .	77
4.22	The path of X-rays within the sample. The incident angle is $\omega$ and the total scattering angle is $2\theta$ . An X-ray with a penetration depth of $z$ is shown. The total thickness of the sample is $t$ . . . . .	79
4.23	NGIWAXS of the DMPC ripple phase for $D = 59.2 \text{ \AA}$ (left) and $60.8 \text{ \AA}$ (right). The angle of incidence $\omega$ was $0.2^\circ$ . The black regions around the edge of each image are the $q$ -space that was not probed. The distorted, non rectangular shape of the probed $q$ -space signifies non-linear relation between the CCD space and sample $q$ -space. . . . .	85

4.24	Enlarged view of the right image in Fig. 4.23. To show smaller features around the peak, a different contrast is used. . . . .	86
4.25	$q_r$ swaths, each averaged over $0.02 \text{ \AA}^{-1}$ . The center $q_z$ value of a swath is shown in the figure legends. . . . .	87

# Chapter 4

## Ripple Phase

When the temperature is reduced from the fluid phase, the ripple phase is observed in bilayers consisting of fully saturated lipids. This chapter discusses X-ray scattering experiments on the ripple phase formed by dimyristolphosphatidylcholine (DMPC) bilayers.

### 4.1 Introduction

(At some point, do some literature search and write up this section) The ripple phase has been a fascinating thermodynamic phase to many physicists and physical chemists since its discovery by Tardieu *et al.* in 1973 [12]. Although this phase has never been reported to occur in a biologically relevant situation, it provides interesting opportunities to study fundamental lipid interactions and their influence on the bilayer shape. (Let's find some recent papers and see if anyone says anything about biological relevance)

The equilibrium structure of the ripple phase has been extensively studied by diffraction (X-ray [] and neutron []) and freeze fracture (electron microscopy [] and scanning tunneling microscopy []) techniques. In the scanning tunneling microscopy experiment [13], the three-dimensional contours of the ripple phase  $P_{\beta'}$  of dimyristolphosphatidylcholine (DMPC) were imaged, and a ripple wavelength of 130 Å and an amplitude of 45 Å were obtained.

Various experiments have indicated the existence of two types of ripple phases: the stable asymmetric and the metastable symmetric phase. In the asymmetric phase, a plane of reflection perpendicular to the ripple wave vector is absent. In the first



systematic study of this phase by Tardieu *et al.*, the X-ray diffraction pattern from DLPC was phased by a pattern recognition technique and the electron density map was calculated. The calculated electron density map showed that the bilayers are height modulated and have a smooth, asymmetric shape. It has been shown that the structure corresponds to a 2D oblique unit cell, the ripple wavelength  $\lambda_r$  is 85.3 Å, the lamellar periodicity  $D$  is 55.3 Å, and the oblique angle  $\gamma$  is 110°. The electron density map has shown that the peak to peak amplitude  $A$  is 15 Å.

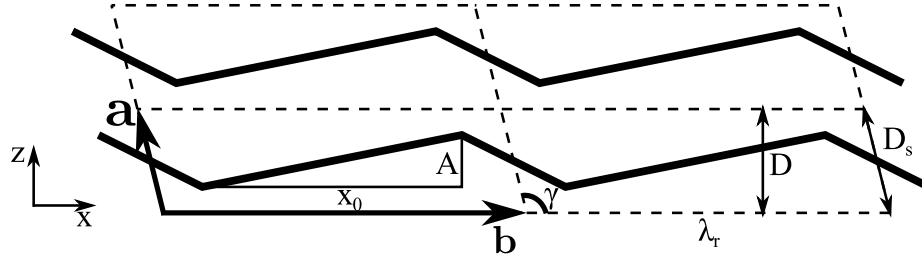


Figure 4.1: Lattice structure of the DMPC ripple phase. Unit cells are shown in dash lines. Center of bilayers are shown by thick, solid lines. Notations in the figure are **a** and **b**: lattice unit vectors,  $D$ :  $D$ -spacing along  $z$ ,  $D_s$ : stacking distance,  $\lambda_r$ : ripple wavelength,  $\gamma$ : oblique tilt angle,  $A$ : ripple amplitude, and  $x_0$ : projected length of the major arm.

From X-ray data of the DMPC ripple of unoriented samples, Wack and Webb has argued that the ripples have a sawtooth shape [1]. Their X-ray form factor data were phased by employing a modeling and fitting technique [14], and the electron density map was calculated, which has shown that the ripples indeed have a sawtooth shape. The map also has shown that the major arm is about twice as long as the minor arm. The bilayer thickness is found to be larger than that of the minor arm. The value of the bilayer thickness in the major arm is comparable to the thickness of DMPC bilayers in the gel phase whereas the thickness of the minor arm is comparable to that in the fluid phase.

A structural investigation by X-ray diffraction of the ripple phase of oriented dipalmitoylphosphatidylcholine (DPPC) samples has indicated that hydrocarbon chains are packed in a hexagonal lattice with chains tilted in the plane perpendicular to the ripple wave vector [15]. In that study, the oblique angle  $\gamma$  was found to be 90°.

Several MD (molecular dynamics) simulations have been carried out, indicating various lipid packing. de Vrie *et al.* has suggested interdigitated chain in the minor side [16].

$D_s$ (Å)	$D$ (Å)	$\lambda_r$ (Å)	$\gamma$ (deg)
55.7	55.0	159.4	99.0
57.5	57.0	140.8	97.6
57.8	57.3	151.6	97.8
57.9	57.4	148.4	97.6
58.0	57.5	144.1	97.8
58.1	57.5	141.9	98.0
58.6	58.0	140.1	98.2
58.6	58.0	141.7	98.4
60.3	59.8	129.6	97.3
61.1	60.6	130.1	97.0
61.9	61.5	130.8	96.5
62.7	62.4	122.0	95.9
64.1	63.9	123.1	94.9
65.0	64.9	120.3	92.3

Table 4.1: Lattice constants for DMPC at  $T = 18.0$  °C reported by Wack and Webb [1].

## 4.2 Materials and Methods

### 4.2.1 Sample Preparation

DMPC was purchased from Avanti Polar Lipids and used without further purification. Oriented thin films were deposited on clean silicon wafers with a chloroform:methanol 2:1 (volume ratio) mixture following the rock and roll procedure. In previous synchrotron experiments, the samples were created and annealed more than a week in advance and stored in a refrigerator. The quality of these samples measured by their mosaic spread was found to worsen over time after the samples were annealed. Therefore, to ensure the best sample quality, the samples were annealed for approximately 12 hours just before the X-ray experiment. Figure 4.2 shows a picture of the annealing chamber. To achieve gentle but efficient hydration of a sample, filter papers were installed covering the sample. For successful annealing, it must be emphasized that the annealing chamber should equilibrate in the annealing oven prior to putting a sample in the chamber. When a sample was put in the chamber sitting at a room temperature and then the system was placed inside the oven, warmer water vapor inside the chamber condensed on the cooler sample, causing so called flooding of oriented sample. A small drop of water on an oriented film is detrimental for the orientation quality because the entropy-driven formation of unilamellar vesicles causes oriented bilayers to peel off one by one.

Figure 4.2: A picture of an annealing chamber. Need to take a picture

The sample for the grazing incident wide angle study was prepared in the same way as for low angle study. In order to minimize the geometric broadening, the sample was trimmed to 1 mm in width along the beam direction.

The sample for transmission study was deposited on a thin, 35 micron, silicon wafer. Because the wafer was very fragile, attaching the sample to a sticky thing was impossible. Instead, the sample was attached to a plastic cap on a small vial with a small amount of heat sink compound at a corner of the wafer. The wafer was stable enough for rocking.

### 4.2.2 Low Angle X-ray Scattering Experiment

The low resolution X-ray scattering experiment was carried out at the Cornell High Energy Synchrotron Source (CHESS) G1 station. The X-ray beam was set up by the station scientist, Dr. Arthor Woll, and the assistant scientist, Dr. Robin lastname?. A W/B<sub>4</sub>C multilayer monochromator with  $\Delta E/E$  of 1.5% was used, providing a very intense X-ray beam. The energy of the X-ray beam was 10.55 keV, corresponding to a wavelength of 1.175 Å. The horizontal and vertical divergence of the beam were  $4.2 \times 10^{-5}$  rad and  $1.6 \times 10^{-4}$  rad, respectively. The beam shape, measured through a semi-transparent 200  $\mu$ m thick molybdenum (Mo) beam stop, is shown in Fig. 4.3 and 4.4. The horizontal beam width was 2.3 pixels (0.16 mm). The vertical beam width was approximately 1 mm, tall enough to cover the entire sample when the sample was tilted by 7°. The sample was rocked during X-ray exposure between -1.6° and 7° in order to observe many diffraction peaks in one data collection. The sample to detector distance was 359.7 mm, measured by indexing silver behenate Bragg peaks. The D-spacing of silver behenate is known to be 58.367 Å.

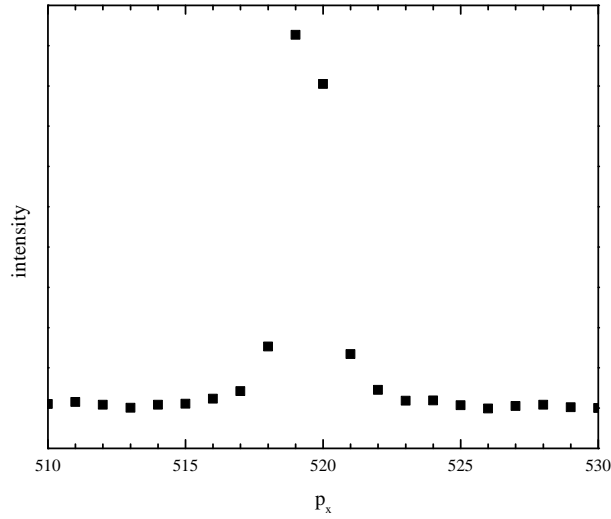


Figure 4.3: The horizontal profile of the beam used in the low resolution study.

A few Bragg peaks in the low angle X-ray scattering of the ripple phase were very strong, leading to saturation of CCD pixels for data collection with a long exposure time. In order to probe a wide range of  $q$ -space, three images were taken: 1) a short,

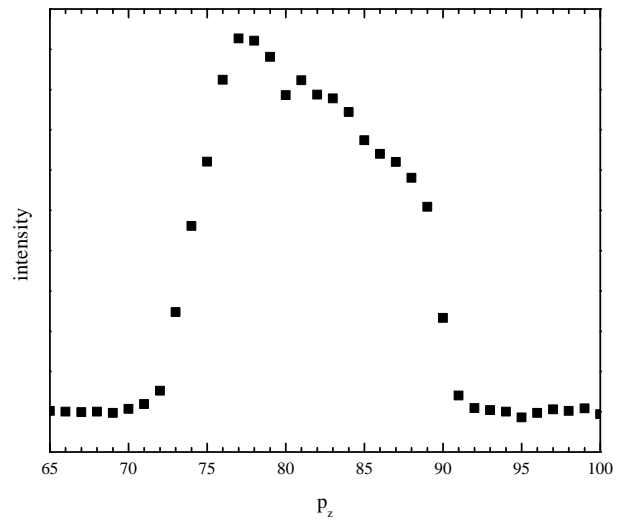


Figure 4.4: The vertical profile of the beam used in the low resolution study.

one second exposure with a nominally 25 micron molybdenum attenuator installed in the upstream of the sample to reduce the intensity of the X-ray beam, 2) one second exposure without the beam attenuator, and 3) 60 second exposure with a beam stop blocking the very intense (1,0) and (2,0) peaks. See Fig. 4.5. Then, the integrated intensity of (1,0) peak was measured from the first image. This value was multiplied by 6.9 to account for the beam attenuation and by 60 to scale with the exposure time. The intensity of (2,0) and (2,-1) were measured from the second image, also multiplied by 60 to account for the shorter exposure time. The intensity of the rest of the observed peaks were measured from the third image.

The integrated intensity of each peak was obtained by putting a box around a peak and summing up the intensity in those pixels that fall inside the box. The background scattering was estimated by measuring the intensity in pixels near the peak but not containing any peak tail. The choice of box size was made according to the width of each peak. Because of mosaic spread in the sample, the peaks were wider for higher orders. Consequently, the box was made wider for higher orders. The box size was chosen so that approximately 80% of the peak intensity was counted toward the integrated intensity.

A thin piece of molybdenum was used to attenuate the beam. The attenuation length  $\mu$  of X-ray in Mo is 6.433  $\mu\text{m}$  for 8 keV and 13.74  $\mu\text{m}$  for 10.55 keV [17]. For a 25  $\mu\text{m}$  thick Mo attenuator,  $\mu = 13.74$  gives the attenuation factor of  $[\exp(-25/13.74)]^{-1} = 6.2$ . The exact attenuation factor was determined by comparing X-ray images collected with and without the attenuator, shown in Fig. 4.6 and 4.7. The attenuation factor of the nominally 25  $\mu\text{m}$  thick Mo was found to be 6.9 for the wavelength used (1.175 Å).

### 4.2.3 Near Grazing Incidence Wide Angle X-ray Scattering Experiment

The high resolution X-ray scattering experiment was also carried out at the G1 station. To achieve a higher instrumental resolution than that for the low angle X-ray scattering experiment described in a previous section, a (111) silicon monochromator was used, which gave  $\Delta E/E$  of 0.01%. Due to the geometry of the G1 station, the Si monochromator was placed in the G1 hutch, in series with the multilayer monochromator. The instrument was set up by the G1 station scientist, Author Woll, and the

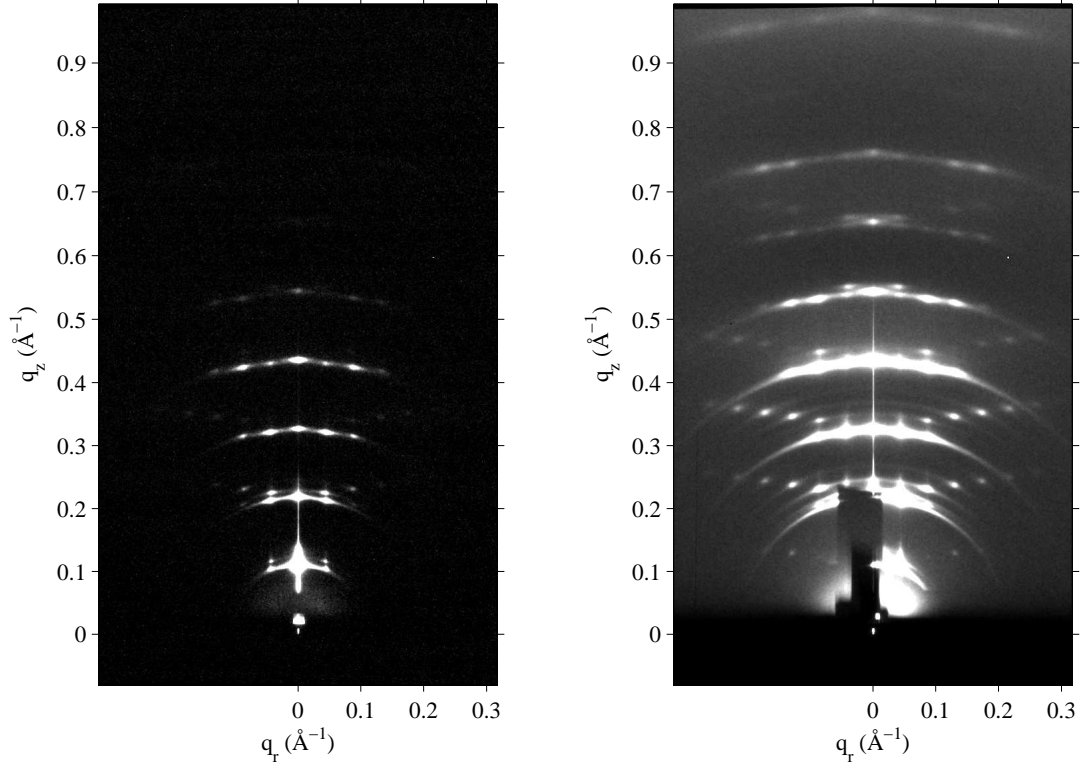


Figure 4.5: 1 second exposure (left) and 60 second exposure (right) of the low angle X-ray scattering from the DMPC ripple phase. The dark rectangle in the right image extending from  $q_z = 0 \text{ \AA}^{-1}$  to  $0.2 \text{ \AA}^{-1}$  is the shadow cast by  $100 \text{ }\mu\text{m}$  thick molybdenum beam stop.  $D = 57.8 \text{ \AA}$ ,  $\lambda_r = 145.0 \text{ \AA}$ , and  $\gamma = 97.8^\circ$ . The gray scales used are  $[0 \text{ } 100]$  (left) and  $[0 \text{ } 500]$  (right).

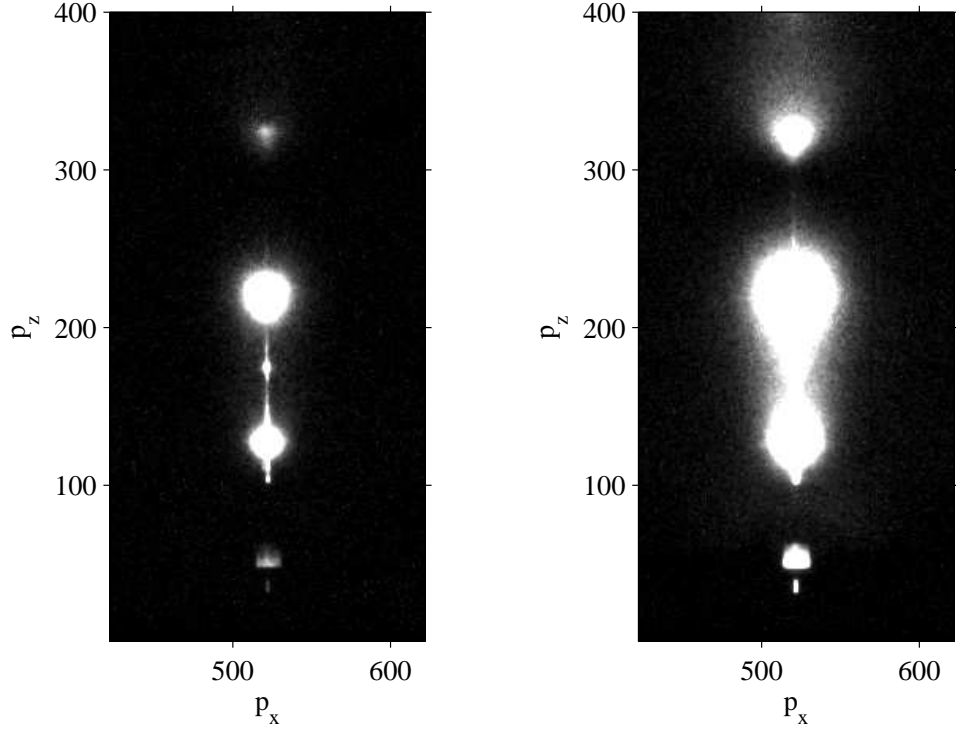


Figure 4.6: CCD images of X-ray scattering taken with (left) and without (right) a nominally  $25\ \mu\text{m}$  thick Mo attenuator. These data were taken at a fixed angle of incidence. The sample was an oriented film of DOPC:DOPE (3:1) in the fluid phase at  $37\ ^\circ\text{C}$ . The wavelength was  $1.175\ \text{\AA}$ , the same as the one used for the ripple phase experiment. The same gray scale is used in both images.

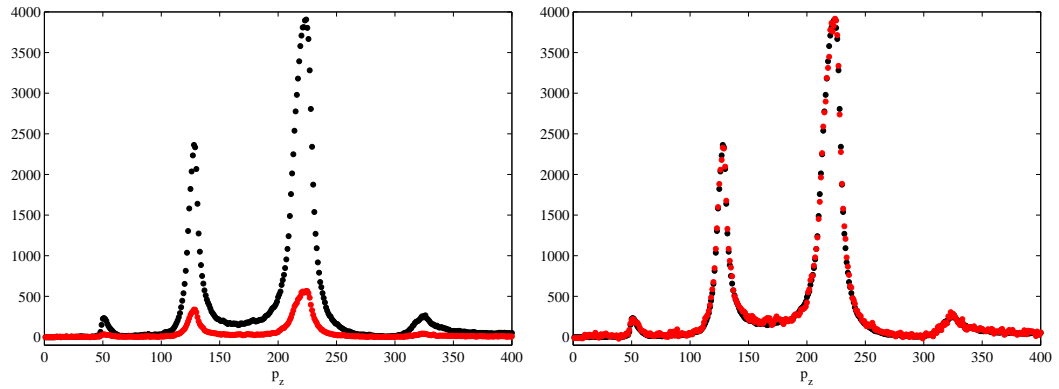


Figure 4.7: Vertical  $p_z$  slices of X-ray images shown in Fig. 4.6 (left). The scattering intensity measured with the attenuator (red solid circles) was multiplied by a factor of 6.9 and compared to the intensity measured without the attenuator (black solid circles, right).



assistant scientist, Dr. Robin lastname.

The energy of the beam was 10.55 keV (wavelength = 1.175 Å). The horizontal and vertical divergence of the X-ray beam were  $4.2 \times 10^{-5}$  rad and  $1.6 \times 10^{-4}$  rad, respectively. The horizontal beam width was 4 pixels (0.28 mm) as shown in Fig. 4.8. With this beam, the scattering resolution in the wide angle region was dominated by the geometric broadening. The broadening was due to the sample width along the beam direction and the horizontal beam width (Fig. 4.9). From the geometry of the experiment, the geometric broadening  $\Delta x$  can be determined,

$$\Delta x = \Delta x_{\text{beam}} + w_s \tan(2\theta).$$

The total scattering angle  $2\theta$  for the ripple WAXS was approximately  $16^\circ$ . To minimize the contribution from the sample, the sample was trimmed to 1 mm along the beam direction. The width of 1 mm was chosen simply because I could not trim more without a more sophisticated device than a simple razor blade. Also, a very narrow sample would be a weak scattering body. Due to limited availability of synchrotron beam time, I considered 1 mm width to be reasonable. With these values, we have  $\Delta x = 0.57$  mm = 8 pixels, which would be the width of a wide angle peak if the correlation length was very large. The sample to detector distance was 220.6 mm, measured using silver behenate. Then, the minimum peak width measured in  $q$ -space would be  $\Delta q \approx 0.014$  Å<sup>-1</sup>. Wide angle X-ray scattering was collected at an incident angle of  $0.2^\circ$ . The total external reflection from an air-lipid interface occurs approximately at  $0.1^\circ$ , so  $0.2^\circ$  is not quite grazing incidence, which usually implies that the incident angle is less than the total reflection angle.

#### 4.2.4 Transmission Wide Angle X-ray Scattering Experiment

The transmission wide angle X-ray scattering (TWAXS) experiment was also carried out at the G1 station, and a similar instrumental resolution to the one used in the low angle experiment was used. The sample to detector distance was measured to be 170 mm using a silver behenate when the angle of incidence  $\omega$  was  $0^\circ$ . The incident angle was set to  $-45^\circ$  for transmission data collection. A 35  $\mu\text{m}$  thick silicon substrate absorbs an X-ray at 10.5 keV by 20% [17]. To measure a D-spacing, mosaic spread of the sample was exploited. Because the axis of the rotation motor did not coincide with the sample axis, the sample to detector distance varied as  $\omega$  was varied. To accurately

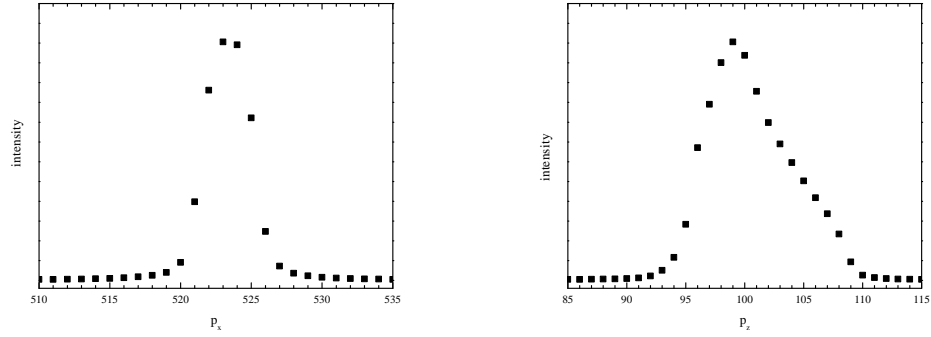


Figure 4.8: Beam used in the high resolution experiment. The horizontal beam profile (left) and vertical beam profile (right) are shown.

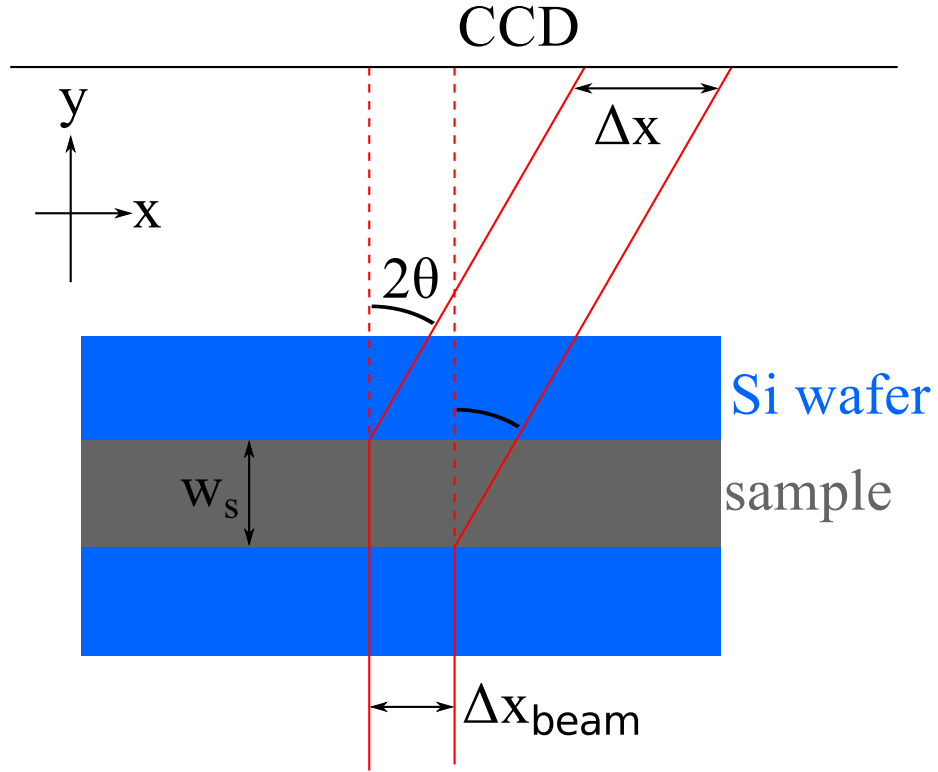


Figure 4.9: The geometric broadening due to the sample width and the beam width. A top view of the sample (gray), Si wafer (blue), and incoming and diffracted X-rays (bounded by red solid lines) are shown. The horizontal beam width is labelled as  $\Delta x_{\text{beam}}$ , the sample width as  $w_s$ , the total scattering angle for a lipid chain-chain correlation as  $2\theta$ , and the geometric broadening as  $\Delta x$ .

measure the sample to detector distance, low angle scattering was collected at a fixed  $\omega$ . Due to the sample mosaic spread, many orders were visible. While the relative intensity of each order was inaccurate, the position of peaks was the same as that observed with a rotating sample. The sample to detector distance was accurately measured at  $\omega = 0^\circ$  using a silver behenate sample. From the geometry of the sample holder, a shift in the sample to detector distance was estimated for an arbitrary incident angle  $\omega$ .

Explain how we estimated the sample to detector distance at  $\omega = -45^\circ$ . Explain how we leveled the sample (using the sample scattering and ascan). The background scattering was collected by replacing the sample with a bare wafer.

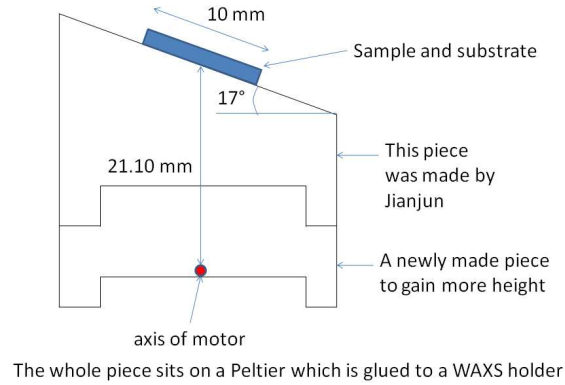


Figure 4.10: Schematics of the sample holder showing a small piece I fabricated

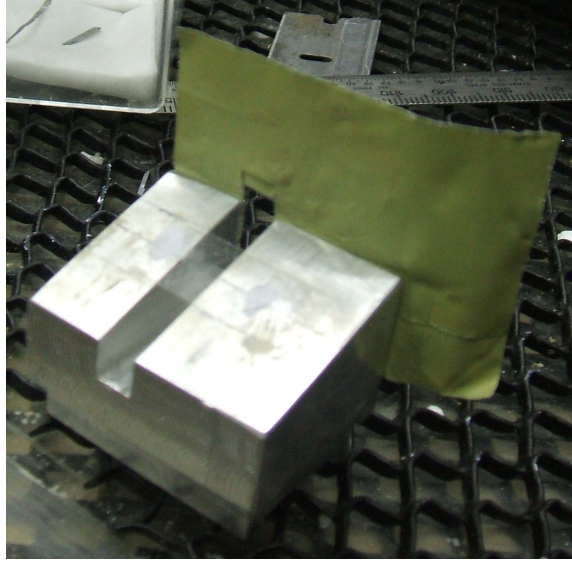


Figure 4.11: Picture of the sample holder looking from the above. A lead tape was attached to the back of the sample holder to help reduce the background scattering, typically coming from the air gap between the flightpath snout and the mylar window of the chamber.

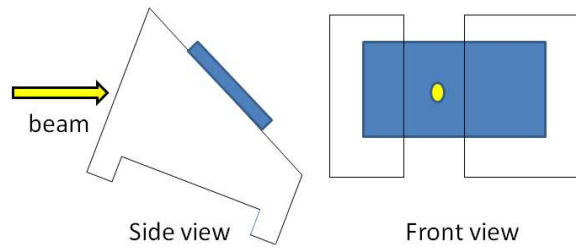


Figure 4.12: Schematics of the sample holder in the transmission mode.

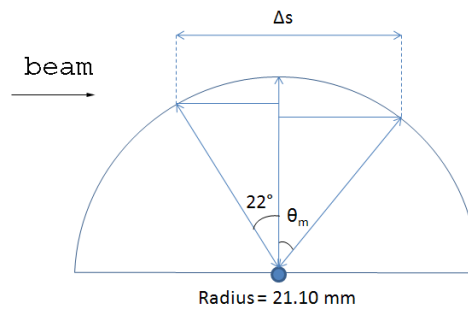


Figure 4.13: Sample holder geometry.

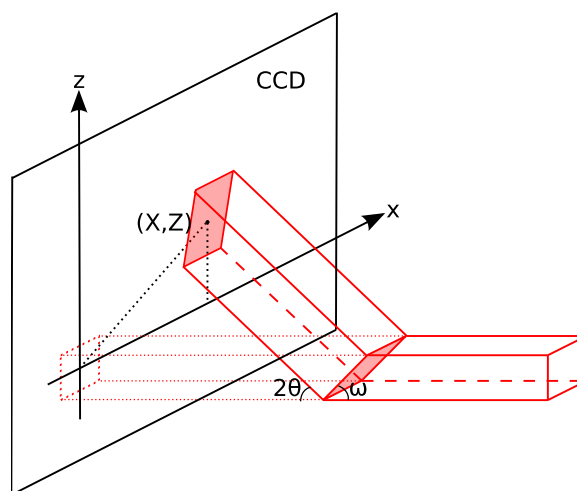


Figure 4.14: Geometric broadening in TWAXS. The cross section of the incoming X-ray with the sample and the CCD detector are both shaded in red.

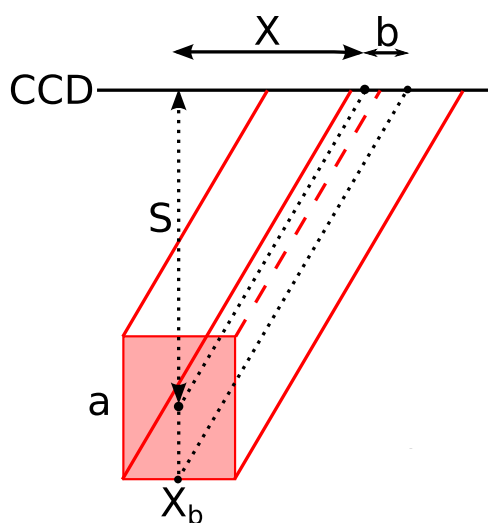


Figure 4.15: Top view of geometric broadening in TWAXS. The cross section of the incoming X-ray with the sample is shaded in red.

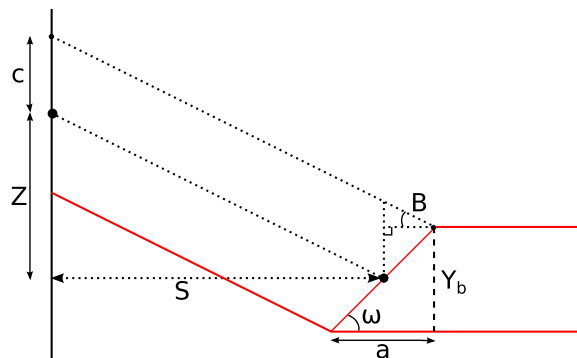


Figure 4.16: Side view of geometric broadening in TWAXS. The cross section of the outgoing X-ray with the CCD detector is shaded in red.

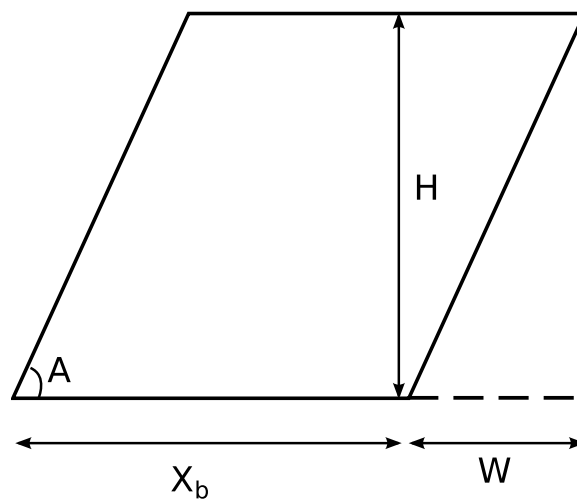


Figure 4.17: Projection of rectangular beam on the detector.

## 4.3 Some Theories

### 4.3.1 Lattice Structure

It has been shown from X-ray studies that ripples in different bilayers are registered to form a two-dimensional oblique lattice as shown in Fig. 4.1. The unit cell vectors in the ripple phase can be expressed as

$$\mathbf{a} = \frac{D}{\tan \gamma} \hat{\mathbf{x}} + D \hat{\mathbf{z}} \quad (4.1)$$

and

$$\mathbf{b} = \lambda_r \hat{\mathbf{x}}. \quad (4.2)$$

The corresponding reciprocal lattice unit cell vectors are

$$\mathbf{A} = \frac{2\pi}{D} \hat{\mathbf{z}} \quad (4.3)$$

and

$$\mathbf{B} = \frac{2\pi}{\lambda_r} \hat{\mathbf{x}} - \frac{2\pi}{\lambda_r \tan \gamma} \hat{\mathbf{z}}. \quad (4.4)$$

The reciprocal lattice vector,  $\mathbf{q}_{hk}$  for the Bragg peak with Miller indices  $(h, k)$  is

$$\mathbf{q}_{hk} = h\mathbf{A} + k\mathbf{B}, \quad (4.5)$$

so its Cartesian components are

$$\mathbf{q}_{hk} \cdot \hat{\mathbf{x}} = q_{hk}^x = \frac{2\pi k}{\lambda_r} \equiv q_k^x \quad (4.6)$$

$$\mathbf{q}_{hk} \cdot \hat{\mathbf{y}} = q_{hk}^y = 0 \quad (4.7)$$

$$\mathbf{q}_{hk} \cdot \hat{\mathbf{z}} = q_{hk}^z = \frac{2\pi h}{D} - \frac{2\pi k}{\lambda_r \tan \gamma}. \quad (4.8)$$

Our sample consists of many ripple domains with varying directions of the ripple wave vector. In this case,  $q_{hk}^x$  and  $q_{hk}^y$  are combined to give  $q_{hk}^r = 2\pi k / \lambda_r$ .

### 4.3.2 Sample $q$ -space

The incoming and outgoing wavevectors of the x-ray beam in Fig. 4.18 are given by

$$\mathbf{k}_{\text{in}} = \frac{2\pi}{\lambda} \hat{\mathbf{y}}, \quad \mathbf{k}_{\text{out}} = \frac{2\pi}{\lambda} (\sin 2\theta \cos \phi \hat{\mathbf{x}} + \cos 2\theta \hat{\mathbf{y}} + \sin 2\theta \sin \phi \hat{\mathbf{z}}), \quad (4.9)$$

where  $\lambda$  is the wavelength of x-ray,  $2\theta$  is the total scattering angle, and  $\phi$  is the angle measured from the equator on the detector. The scattering vector (also called momentum transfer vector) is the difference between  $\mathbf{k}_{\text{in}}$  and  $\mathbf{k}_{\text{out}}$ ,

$$\begin{aligned} \mathbf{q} &= \mathbf{k}_{\text{out}} - \mathbf{k}_{\text{in}} \\ &= q (\cos \theta \cos \phi \hat{\mathbf{x}} - \sin \theta \hat{\mathbf{y}} + \cos \theta \sin \phi \hat{\mathbf{z}}), \end{aligned} \quad (4.10)$$

where  $q = 4\pi \sin \theta / \lambda$  is the magnitude of the scattering vector. When the sample is rotated by  $\omega$  about the lab x-axis in the clockwise direction as shown in Fig. 4.18, the sample  $q$ -space also rotates and are given by

$$\hat{\mathbf{e}}_{\mathbf{x}} = \hat{\mathbf{x}}, \quad \hat{\mathbf{e}}_{\mathbf{y}} = \cos \omega \hat{\mathbf{y}} + \sin \omega \hat{\mathbf{z}}, \quad \hat{\mathbf{e}}_{\mathbf{z}} = -\sin \omega \hat{\mathbf{y}} + \cos \omega \hat{\mathbf{z}}. \quad (4.11)$$

From Eq. (4.10) and (4.11), we find Cartesian components of the sample  $q$ -space to be

$$\begin{aligned} q_x &= \mathbf{q} \cdot \hat{\mathbf{e}}_{\mathbf{x}} = q \cos \theta \cos \phi, \\ q_y &= \mathbf{q} \cdot \hat{\mathbf{e}}_{\mathbf{y}} = q (-\sin \theta \cos \omega + \cos \theta \sin \phi \sin \omega), \\ q_z &= \mathbf{q} \cdot \hat{\mathbf{e}}_{\mathbf{z}} = q (\sin \theta \sin \omega + \cos \theta \sin \phi \cos \omega). \end{aligned} \quad (4.12)$$

The position,  $(X, Z)$ , of a CCD pixel is measured with respect to the beam and given by

$$X = S \tan 2\theta \cos \phi, \quad Z = S \tan 2\theta \sin \phi, \quad (4.13)$$

where  $S$  is the distance between the sample and detector.

From a model for the electron density of a lipid bilayer, one calculates a X-ray scattering intensity pattern,  $I(\mathbf{q})$ . Then, Eq. (4.12) and (4.13) relate  $I(\mathbf{q})$  to the experimentally measured intensity pattern,  $I(X, Z)$ . It is important to remember that a given pixel position,  $(X, Z)$ , corresponds to a triplet  $(q_x, q_y, q_z)$ . Fully exploring the sample  $q$ -space requires changing  $\omega$  for a fixed wavelength, which was achieved



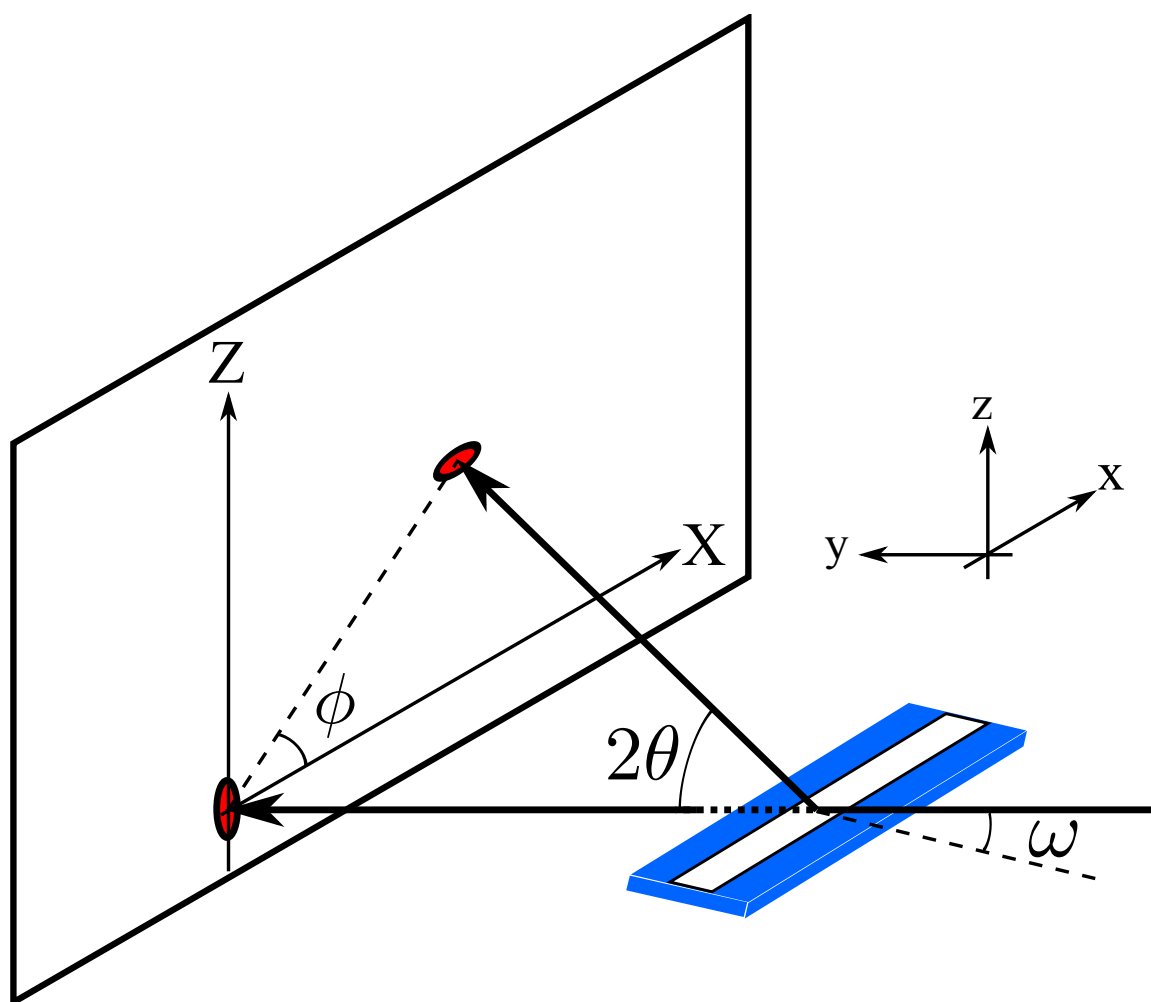


Figure 4.18: Experimental reflectivity geometry.

by continuously rotating the sample with a motor. In the ripple phase, because our sample has in-plane rotational symmetry, the ripple side peaks make up Bragg rings while the main peaks are still delta function like (see Fig. X) in  $q$ -space. In order for the main peak to be observed,  $\omega$  must be equal to  $\theta_B$ , but the side peaks are observed at any  $\omega$ . Those side peaks get slightly smeared due to integration over  $q_y$ .

For low angle x-ray scattering (LAXS), it is convenient to linearize the above equations in terms of  $\theta$  and  $\omega$ . In the small angle approximation,  $\sin \phi \approx Z/(2S\theta)$  and  $\cos \phi \approx X/(2S\theta)$ , and

$$\begin{aligned} q_x &\approx \frac{4\pi\theta \cos \phi}{\lambda} \approx kX/S \\ q_y &\approx q_z\omega - \frac{4\pi\theta^2}{\lambda} \approx q_z\omega - \frac{\lambda q_z^2}{4\pi} \\ q_z &\approx \frac{4\pi\theta \sin \phi}{\lambda} \approx kZ/S, \end{aligned} \tag{4.14}$$

with  $k = 2\pi/\lambda$ . For wide angle X-ray scattering, the exact relations given by Eq. (4.12) are necessary. Especially in the transmission experiment, where  $\omega$  is large, an observed X-ray pattern appears nontrivial and becomes almost impossible to analyze without the use of Eq. (4.12).

### 4.3.3 Lorentz Correction

Our sample has in-plane rotational symmetry. This means that the sample consists of many domains with differing ripple directions, all domains being parallel to the substrate. In sample  $q$ -space, ripple  $k \neq 0$  side peaks are represented as rings centered at the meridian, or  $q_z$ -axis, while  $k = 0$  peaks are still points on the meridian (see Fig. 4.19). Then, for an arbitrary incident angle,  $k = 0$  peaks are not observed while side peaks are observed. In order to capture both  $k = 0$  and  $k \neq 0$  side peaks in one X-ray exposure, the sample was continuously rotated. As a result of this rotation,  $k = 0$  peaks become arcs that subtend an angle  $2\theta_{h0}$ , as shown in Fig. 4.20, with its length equal to  $2\theta_{h0}q_{h0}^z$ .

The detector records the intersections of these arcs with the Ewald sphere, so the total scattering intensity is the product of the observed intensity,  $I_{hk}^{\text{obs}}$  with the arc length, that is,

$$I = 2\theta_{h0}q_{h0}^z I_{h0}^{\text{obs}}. \tag{4.15}$$

Because the sample has in-plane rotational symmetry,  $k \neq 0$  side peaks are represented as rings whose radius is  $q_{hk}^r$ . Because only the domains with the right ripple direction can satisfy the Bragg's condition at a given fixed angle, the scattering intensity from a domain is reduced by a factor of  $2\pi q_k^r$  compared to  $h = 0$  peaks to which all domains contribute simultaneously at the Bragg angle. This reduction of intensity can be nicely visualized by the Ewald sphere construction, which shows that the entire rings are not intersected by the Ewald sphere at a fixed angle. During an X-ray exposure, the sample  $q$ -space rotates and the rings are intersected by the Ewald sphere at all incident angles. However, as Fig. 4.21 shows, only small parts of the rings are actually intersected with the Ewald sphere. Then, the total scattering intensity is given by

$$I = 2\pi q_k^r I_k^{\text{obs}}. \quad (4.16)$$

Inverting Eq. (4.15) and (4.16) and realizing that the intensity is the form factor squared, we can calculate the observed intensity,  $I_{hk}^{\text{obs}}$ , from a model for an electron density in the ripple phase.

Mathematically, the rotation is equivalent to an integration over  $\omega$ . In low angle X-ray scattering,  $q_z$  is constant at a given pixel as  $\omega$  is changed, which can be seen from Eq. (4.14).  $\omega$  dependence appears only through  $q_y$ , so rotating the sample is realized by integrating over  $q_y$ . To derive the integration limits, let us consider two cases: (a) When  $\omega \leq 0$ , the incoming X-ray beam is blocked by the back of the substrate. This sets the lower limit to 0. (b) When  $\omega \geq 2\theta$ , the substrate blocks the outgoing X-ray. Within the small angle approximation, then,  $\omega_{\text{max}}$  is  $2 \times \lambda q_z / (4\pi)$  for scattering with  $q_z$ . Thus, the integration limits for  $q_y$  integration are  $[-\lambda q_z^2 / (4\pi), \lambda q_z^2 / (4\pi)]$ . We also need to integrate over  $X$  and  $Z$  to obtain integrated intensity. From Eq. 4.14, we see that  $d\omega = dq_y / q_z$  for a fixed  $q_z$  value. Using Eq. 4.14, these lead to the observed intensity written as,

$$\begin{aligned} I_{hk}^{\text{obs}} &\propto \int dX \int dZ \int d\omega |F_{hk}|^2 S_{hk}(\mathbf{q}) \\ &\propto |F_{hk}|^2 \int dq_x \int dq_z \int_{-\frac{\lambda q_z^2}{4\pi}}^{\frac{\lambda q_z^2}{4\pi}} \frac{dq_y}{q_z} S_{hk}(\mathbf{q}), \end{aligned} \quad (4.17)$$

where  $1/q_z$  factor in  $q_y$  integration is the Lorentz polarization factor in the small angle approximation. The second line in Eq. 4.17 is derived anticipating that  $q_z$  is

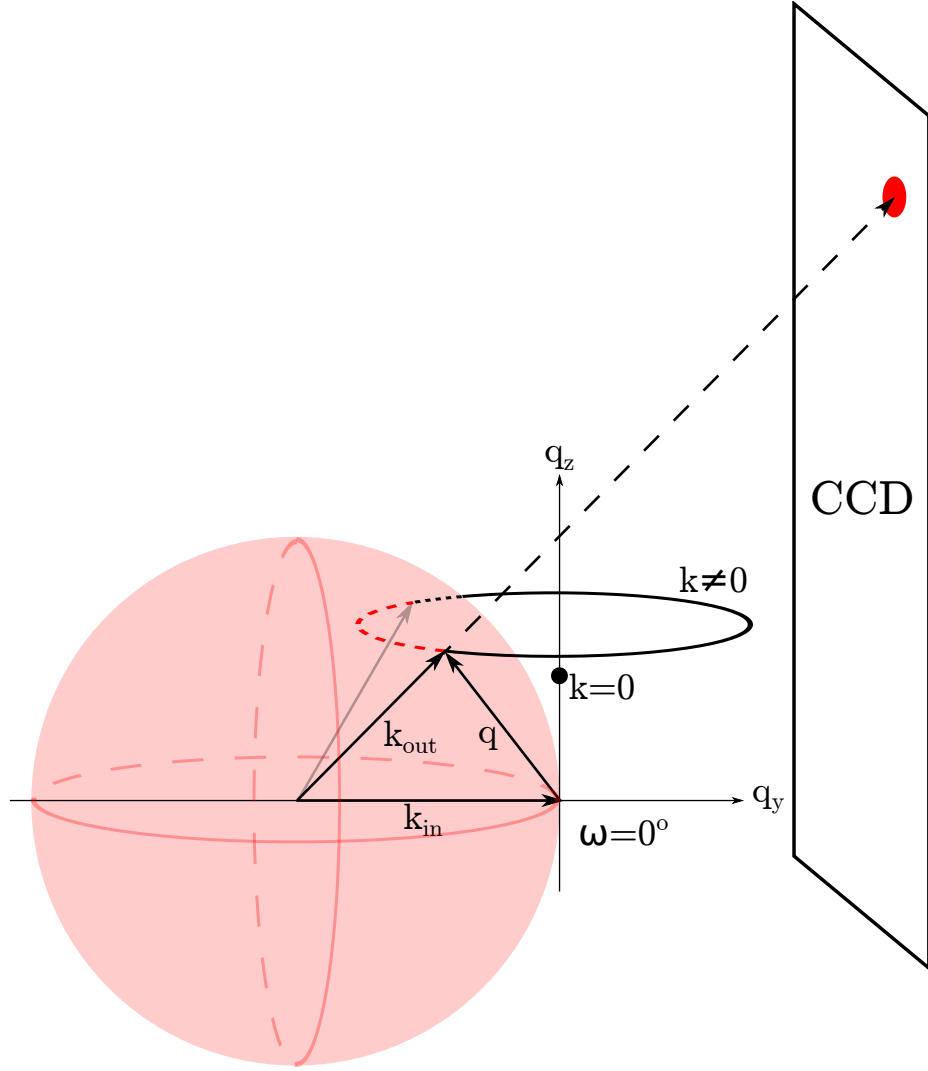


Figure 4.19: Ewald sphere construction for the ripple phase diffraction in the low angle regime. A ripple  $k = 0$  peak is the solid, black circle on the  $q_z$ -axis. A ripple  $k \neq 0$  ring is the black ring centered about the  $q_z$ -axis. The portion of the ring that is inside the Ewald sphere is shown as a red dashed line and the portion of the ring that is outside but behind the Ewald sphere is shown as a black dotted line. The magnitude of the total scattering angle is exaggerated. With a wavelength of  $1.175 \text{ \AA}$ , the magnitude  $|\mathbf{k}_{\text{in}}| = 5.35 \text{ \AA}^{-1}$ . For a  $h = 5$  peak,  $q_{50}^z = 0.54 \text{ \AA}^{-1}$ , one tenth of  $k_{\text{in}}$ .

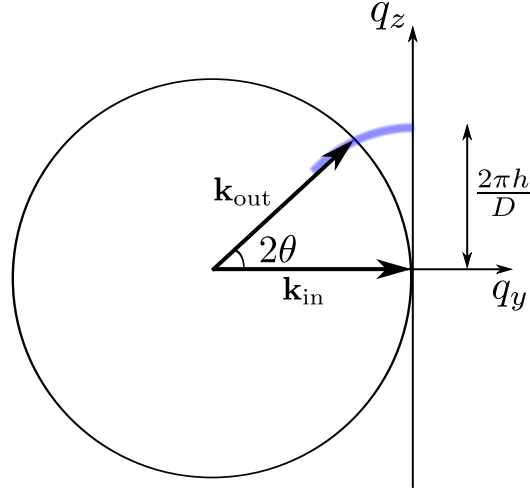


Figure 4.20: Side view of an arc of  $k = 0$  peak shown as a light blue line.

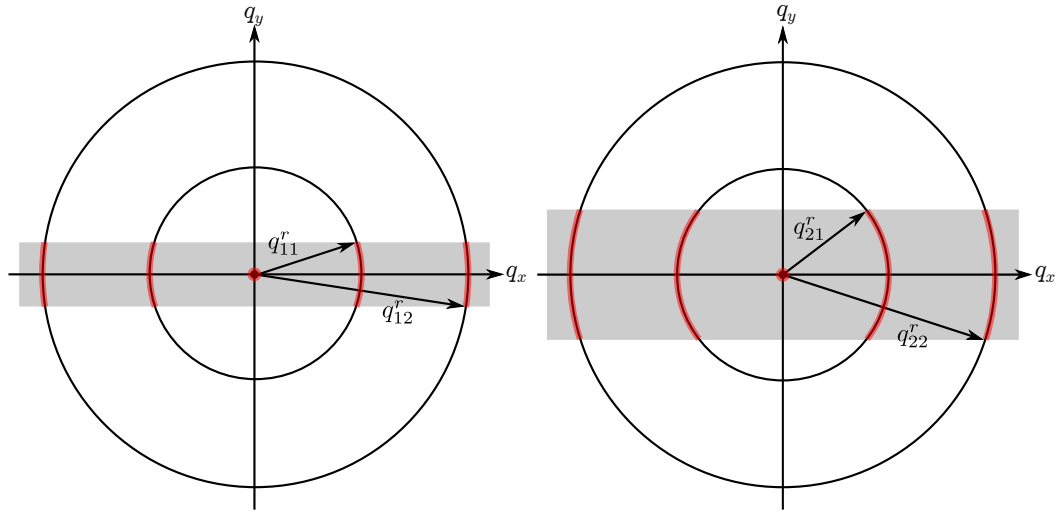


Figure 4.21:  $q$ -space representations of Bragg peaks and Bragg rings for  $h = 1$  and  $k = 0, 1$ , and  $2$  in  $q_{hk}^z$  planes. The shaded rectangles show cross sections of the rotating Ewald sphere along  $q_{hk}^z$  plane. The intersection between the Ewald sphere and a Bragg peak/ring is indicated in red. The observed intensity for the  $k \neq 0$  orders is proportional to the fraction of the length of red arcs in the circumference. This fraction is equal to one for a  $k = 0$  order. Because the orders are not in the same  $q_z$  plane, the range of  $q_y$  integration indicated by the height of the rectangle is different for different orders. The magnitude of curvature of arcs is exaggerated.

a constant for any Bragg orders, so that  $q_z$  integration simply replaces  $q_z$  variables with  $q_{hk}^z$ .

For a crystalline sample with the in-plane rotational symmetry, the structure factor of a ripple Bragg peak is

$$S_{hk}(\mathbf{q}) = S_{hk}(q_r, q_z) = \frac{1}{2\pi q_r} \delta(q_r - q_{r,k}) \delta(q_z - q_{z,hk}), \quad (4.18)$$

where  $q_{r,k} = 2\pi|k|/\lambda_r$ . Thus, the scattering pattern in the ripple phase is a collection of Bragg “rings” centered at the meridian and the Bragg peaks located along the meridian. The observed, integrated intensity of  $hk$  peak is proportional to

$$I_{o,hk} \propto \frac{|F_{hk}|^2}{q_{z,hk}} \int dq_x \int_{-q_{y0}}^{q_{y0}} dq_y \frac{\delta(q_r - q_{r,k})}{2\pi q_r}, \quad (4.19)$$

where  $q_{y0} = \lambda q_{z,hk}^2 / (4\pi)$ . For side peaks ( $k \neq 0$ ), we have

$$\begin{aligned} \int dq_x \int_{-q_{y0}}^{q_{y0}} dq_y \frac{\delta(q_r - q_{r,k})}{2\pi q_r} &\approx \int_{-\frac{q_{y0}}{q_{r,k}}}^{\frac{q_{y0}}{q_{r,k}}} d\phi \int dq_r q_r \frac{\delta(q_r - q_{r,k})}{2\pi q_r} \\ &= \frac{q_{y0}}{\pi q_{r,k}}. \end{aligned} \quad (4.20)$$

For main peaks ( $k = 0$ ), we have

$$\begin{aligned} \int dq_x \int_{-q_{y0}}^{q_{y0}} dq_y \frac{\delta(q_r - q_{r,k})}{2\pi q_r} &= \int_0^{2\pi} d\phi \int dq_r q_r \frac{\delta(q_r - q_{r,k})}{2\pi q_r} \\ &= 1 \end{aligned} \quad (4.21)$$

Using Eq. (4.20) and (4.21), we write the observed integrated intensity as

$$I_{o,h0} \propto \frac{|F_{h0}|^2}{q_{z,h0}} \quad (4.22)$$

$$I_{o,hk} \propto \frac{|F_{hk}|^2}{q_{z,hk}} \frac{q_{y0}}{\pi q_{r,k}} = |F_{hk}|^2 \frac{\lambda q_{z,hk}}{2\pi} \frac{1}{2\pi q_{r,k}} = |F_{hk}|^2 \frac{2\theta_{hk}}{2\pi q_{r,k}}, \quad (4.23)$$

where  $2\theta_{hk} = \lambda q_{z,hk} / (2\pi)$  is the incident angle at which the outgoing X-ray for the peak ( $hk$ ) is blocked by the substrate. Eq. (4.22) and (4.23) relate the form factor calculated from a model to the experimentally observed intensity, and are equivalent

to Eq. (4.15) and (4.16), which were derived by using the Ewald sphere.

In non-linear least squares fitting procedure, we fitted the observed integrated intensity to the calculated intensity from a bilayer model using these geometrical corrections. This is because we can determine experimental uncertainties on observed intensity rather than the geometrically corrected form factors. We avoid propagating the uncertainties by fitting a model to observed intensity.

#### 4.3.4 Absorption Correction for LAXS

(Under construction) In this section, we derive the absorption correction for the thin film sample. The calculation involves an explicit integration over the incident angle,  $\omega$ , which is necessiated by the sample rotation during an x-ray exposure. The procedure is to write down an absorption factor,  $A(\omega, \theta)$ , for a given scattering angle at a given incident angle, and then integrate over  $\omega$ . We ignore  $q_x$  dependence because the X-ray path inside the sample is nearly within the  $y$ - $z$  plane for low angle scattering. The correction for wide angle scattering is described in a later section.

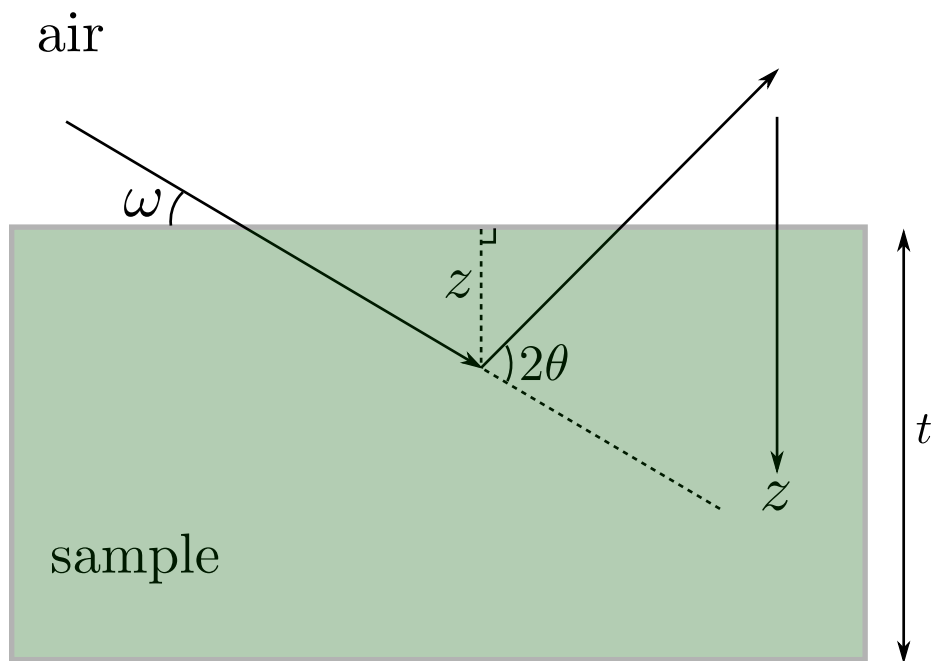


Figure 4.22: The path of X-rays within the sample. The incident angle is  $\omega$  and the total scattering angle is  $2\theta$ . An X-ray with a penetration depth of  $z$  is shown. The total thickness of the sample is  $t$ .

Assume that all the X-rays enter the sample from the top surface. The total

scattering angle is given by  $2\theta$  (see Fig. 4.22). Let  $z$ -axis point downward. At the top surface (air-sample interface),  $z = 0$ . For X-rays that travel to  $z$  and then scatter, the total path length within the sample is

$$L_{\text{tot}}(z, \omega, \theta) = \frac{z}{\sin \omega} + \frac{z}{\sin(2\theta - \omega)} = zg(\omega, \theta), \quad (4.24)$$

where  $g(\omega, \theta) = (\sin \omega)^{-1} + (\sin(2\theta - \omega))^{-1}$ . For each ray, the intensity is attenuated by the sample absorption. If non-attenuated intensity is equal to  $I_0$ , then the attenuated intensity is

$$I(z, \omega, \theta) = I_0 \exp\left(-\frac{L_{\text{tot}}}{\mu}\right), \quad (4.25)$$

where  $\mu$  is the absorption length of an X-ray.  $\mu$  is 111 for 10.5 keV and 222 for 8 keV [17]. The observed intensity of scattering from a sample fixed at an angle  $\omega$  is equal to the integration of Eq. (4.25) over the whole sample and given by

$$\begin{aligned} I_{\text{obs}}(\omega, \theta) &= \int_0^t dz I(z, \omega, \theta) = I_0 \int_0^t dz \exp\left(-\frac{g(\omega, \theta)}{\mu} z\right) \\ &= I_0 \mu \frac{1 - \exp\left(-\frac{t}{\mu} g(\omega, \theta)\right)}{g(\omega, \theta)}. \end{aligned} \quad (4.26)$$

Defining the absorption factor at a fixed angle to be  $A(\omega, \theta)$ , the observed intensity can be written as

$$I_{\text{obs}}(\omega, \theta) = A(\omega, \theta) t I_0, \quad (4.27)$$

where  $tI_0$  is the intensity we would observe for non-absorbed X-rays. Equating Eq. (4.26) and (4.27), we get

$$A(\omega, \theta) = \frac{\mu}{t} \frac{1 - \exp\left(-\frac{t}{\mu} g(\omega, \theta)\right)}{g(\omega, \theta)}. \quad (4.28)$$

The total observed intensity from a sample that is being rotated during an exposure is simply

$$I_{\text{total}}(\theta) = \int_0^{2\theta} d\omega I_{\text{obs}}(\omega, \theta). \quad (4.29)$$

The upper integration limit is equal to  $2\theta$  because the substrate completely blocks the scattered X-rays above this angle as discussed in section 4.3.3.



Because the total non-attenuated intensity is given by  $t\omega I_0$ ,  
so that the total absorption factor is equal to

$$A(\theta) = \frac{\mu}{2\theta t} \int_0^{2\theta} d\omega \frac{1 - \exp\left(-\frac{t}{\mu}g(\omega)\right)}{g(\omega)}. \quad (4.30)$$

If  $\mu$  is taken to infinity (no absorption),  $A$  goes to 1 as expected. Here, it is important to note that  $1/2\theta$  factor in the above equation is normally called Lorentz polarization factor, which is usually approximated as  $1/q_z$  for LAXS analysis. Since the SDP program applies this correction factor in addition to the absorption correction, we remove this factor in the formula for  $A_c$ . Therefore, the final result for the total absorption correction is

$$A_c(\theta) = \frac{1}{2\theta A(\theta)} = \frac{t}{\mu} \left[ \int_0^{2\theta} d\omega \frac{1 - \exp\left(-\frac{t}{\mu}g(\omega)\right)}{g(\omega)} \right]^{-1}$$

with  $g(\omega) = 1/\sin \omega + 1/\sin(2\theta - \omega)$ .

### 4.3.5 Absorption Correction for WAXS

(Under construction)

### 4.3.6 Effect of mosaic spread

(Under construction)

## 4.4 Model

### 4.4.1 Contour Part of the Form Factor

As in ref, we take the ripple profile to have a sawtooth-like profile. Its amplitude is  $A/2$  and the projection of the major arm on the ripple direction is  $x_0$  as shown in

Fig. X. Then, we write the ripple profile as

$$u(x) = \begin{cases} -\frac{A}{\lambda_r - x_0} \left(x + \frac{\lambda_r}{2}\right) & \text{for } -\frac{\lambda_r}{2} \leq x < -\frac{x_0}{2}, \\ \frac{A}{x_0} x & \text{for } -\frac{x_0}{2} \leq x \leq \frac{x_0}{2}, \\ -\frac{A}{\lambda_r - x_0} \left(x - \frac{\lambda_r}{2}\right) & \text{for } \frac{x_0}{2} < x \leq \frac{\lambda_r}{2}. \end{cases} \quad (4.31)$$

The ripple profile has the inversion symmetry, so that the resulting form factor is real.  $A$  and  $x_0$  are fitting parameters that depend on the integrated intensity of each peak while  $D$  and  $\lambda_r$  are determined from measuring the positions of the Bragg peaks.

In order to allow the electron density along the ripple direction to modulate, we include two additional parameters, one to allow for the electron density across the minor side to be different by a ratio  $f_1$  from the electron density across the major side and a second parameter  $f_2$ , which is multiplied by  $\delta$  functions  $\delta(x \pm x_0/2)$  to allow for a different electron density near the kink between the major and the minor sides.

#### 4.4.2 Transbilayer Part of the Form Factor

##### SDF

Delta function model is described here.

##### 2G model

In the hybrid model, the terminal methyl region of the bilayer is represented as a Gaussian function [18]. The headgroups are represented by one and two Gaussian functions in 1G and 2G hybrid model, respectively. The methylene and water regions are each treated as a constant. The gap between the two constants is represented by a sine function. Then, for half of the bilayer,  $0 \leq z \leq D/2$ , the electron density has the form,

$$\rho(z) = \rho_G(z) + \rho_S(z) + \rho_B(z), \quad (4.32)$$

where the Gaussian part is given by

$$\rho_G(z) = \sum_{i=1}^{1 \text{ or } 2} \rho_{Hi} e^{-(z-Z_{Hi})^2/(2\sigma_{Hi}^2)} + \rho_M e^{-z^2/(2\sigma_M^2)}, \quad (4.33)$$

the strip part is given by

$$\rho_S(z) = \begin{cases} \rho_{CH_2} & \text{for } 0 \leq z < Z_{CH_2}, \\ \rho_W & \text{for } Z_W \leq z \leq D/2, \end{cases} \quad (4.34)$$

and the bridging part is given by

$$\rho_B(z) = \frac{\rho_W - \rho_{CH_2}}{2} \cos \left[ \frac{-\pi}{\Delta Z_H} (z - Z_W) \right] + \frac{\rho_W + \rho_{CH_2}}{2} \quad \text{for } Z_{CH_2} < z < Z_W. \quad (4.35)$$

with  $\Delta Z_H = Z_W - Z_{CH_2}$ . Here, we assume  $Z_{H2} > Z_{H1}$ . Table 4.2 shows some of the definitions. The transbilayer profile along  $x = -z \tan \psi$  can be obtained by rotating

	1G	2G
$Z_{CH_2}$	$Z_{H1} - \sigma_{H1}$	$Z_{H1} - \sigma_{H1}$
$Z_W$	$Z_{H1} + \sigma_{H1}$	$Z_{H2} + \sigma_{H2}$

Table 4.2: Definitions of  $Z_{CH_2}$  and  $Z_W$

the coordinates  $x$  and  $z$  by  $\psi$  in the clockwise direction and reexpressing  $\rho(z)$  in terms of the rotated coordinates. This leads to replaing  $x$  with  $x' = x \cos \psi + z \sin \psi$  and  $z$  with  $z' = -x \sin \psi + z \cos \psi$ . Then, the rotated transbilayer profile is

$$\rho(x, z) = \delta(x + z \tan \psi) [\rho_G(z') + \rho_S(z') + \rho_B(z')]. \quad (4.36)$$

Taking the two dimensional Fourier transform of Eq. (4.36) leads to the transbilayer part of the form factor,

$$F_T = \int_{-\frac{D}{2}}^{\frac{D}{2}} \int_{-\frac{\lambda_T}{2}}^{\frac{\lambda_T}{2}} [\rho(x, z) - \rho_W] e^{i(q_x x + q_z z)} dx dz \quad (4.37)$$

$$= F_G + F_S + F_B. \quad (4.38)$$

The form factor is calculated in the minus fluid convention, where the bilayer electron density is measured with respect to the electron density of the surrounding solvent. The expression for  $F_T$  is rather messy and not shown. The derivation and full expression can be found in the appendix. Here, we note that the fitting parameters in this model are  $Z_{Hi}$ ,  $\sigma_{Hi}$ , and  $R_{HiM}$  for each of the two headgroup Gaussian functions,  $\sigma_M$  for the terminal methyl Gaussian,  $\Delta R$  for the methylene region,  $\psi$  for the lipid

tilt, and an overall scaling factor. The contour part of the form factor has four more parameters ( $A$ ,  $x_0$ ,  $f_1$ , and  $f_2$ ). In total, the modified 2G hybrid model implements 14 structural parameters.

## 4.5 Results

### 4.5.1 Data and Electron Density Profile

Table 4.3 summarizes data we analyzed. As shown, we measured scattering in a almost identical conditions as the Wack and Webb's. This data allowed us to check our data obtained by using an oriented sample against an unoriented sample. As discussed earlier, these two types of samples give different Lorentz correction. We derived the Lorentz correction for our oriented sample.

	$\lambda_r$	$D$	$\gamma$
WW	141.7	57.94	98.4°
S1	145	57.8	98.2°
S2	?	?	?

Table 4.3: Lattice constants

Show a table showing our measured form factor (Lorentz corrected). Do the fits once we decide on mosaic spread correction. Show in a table, fitting results. Show an edp. Show the thicknesses of both arms. Comment on some fine features.

### 4.5.2 Near Grazing Incidence Wide Angle X-ray Scattering (NGIWAXS)

Figure 4.23 shows near grazing incidence Wide Angle X-ray scattering (NGIWAXS) from an oriented DMPC film in the ripple phase. As can be seen, hydrocarbon chain scattering did not vary considerably between the two  $D$ -spacings. A weak feature that looks like an arc coming from the chain peak was observed. This feature extended out from  $\phi = 0^\circ$  to at least  $70^\circ$ . This feature might simply be mosaic spread scattering due to the peak near the equator. Because mosaic spread of this sample was very small, it may also be possible that the feature is not mosaic spread arc, but comes from the minor arm, indicating that tilt modulation may occur in the minor arm. Chains

are packed quite tightly, unlike in the fluid phase. (I did rocking scan, so show the data, and maybe estimate what scattering would look like based on Lorentzian distribution.)

Figure 4.24 shows an enlarged image of the ripple phase WAXS at  $D = 60.8$  Å. We observed a strong peak off the equator and a weak one, the center of which was not determined. The maximum intensity of the strong peak was at  $(q_r, q_z) \approx (1.49 \text{ Å}^{-1}, 0.19 \text{ Å}^{-1})$  as shown in Fig. 4.25. The weak peak was observed near the equator, but separation of this peak from the strong one was most visible at  $q_z = 0.13 \text{ Å}^{-1}$  as Fig. 4.25 shows. Separation of the two peaks was possible because of the high resolution experiment. In previous runs with the low resolution setup, the ripple peak appeared as a single wide peak.

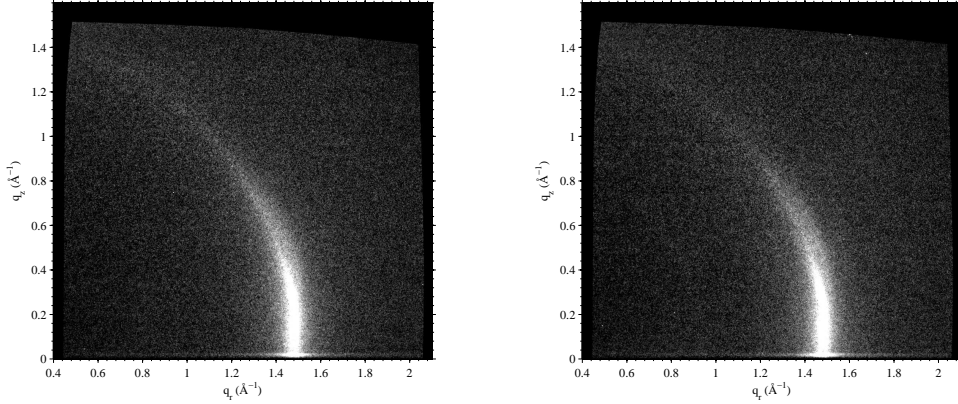


Figure 4.23: NGIWAXS of the DMPC ripple phase for  $D = 59.2$  Å (left) and  $60.8$  Å (right). The angle of incidence  $\omega$  was  $0.2^\circ$ . The black regions around the edge of each image are the  $q$ -space that was not probed. The distorted, non rectangular shape of the probed  $q$ -space signifies non-linear relation between the CCD space and sample  $q$ -space.

(some thought) Can we say that the observed arc like scattering is not the mosaic spread, but true sample scattering? Comment on the widths of the peaks observed. Possibly make use of both low and high resolution data. Apply the absorption correction. Show  $q$  swaths for various  $\phi$ .

### 4.5.3 Transmission WAXS

Convert the image to  $q$ -space. No strong order on the equator. Compare to NGIWAXS and comment on the absorption effect in NGIWAXS data.

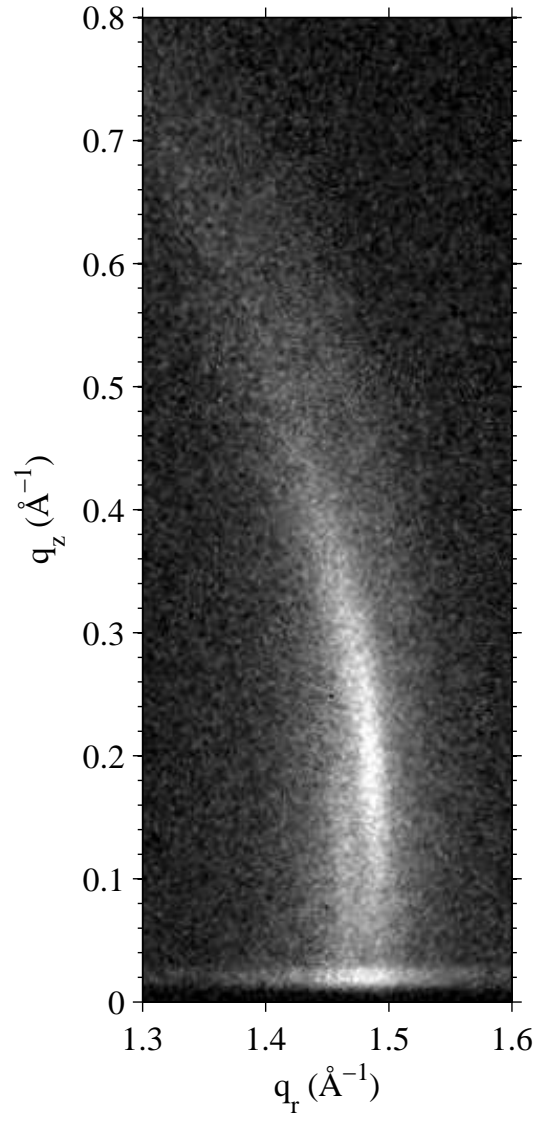


Figure 4.24: Enlarged view of the right image in Fig. 4.23. To show smaller features around the peak, a different contrast is used.

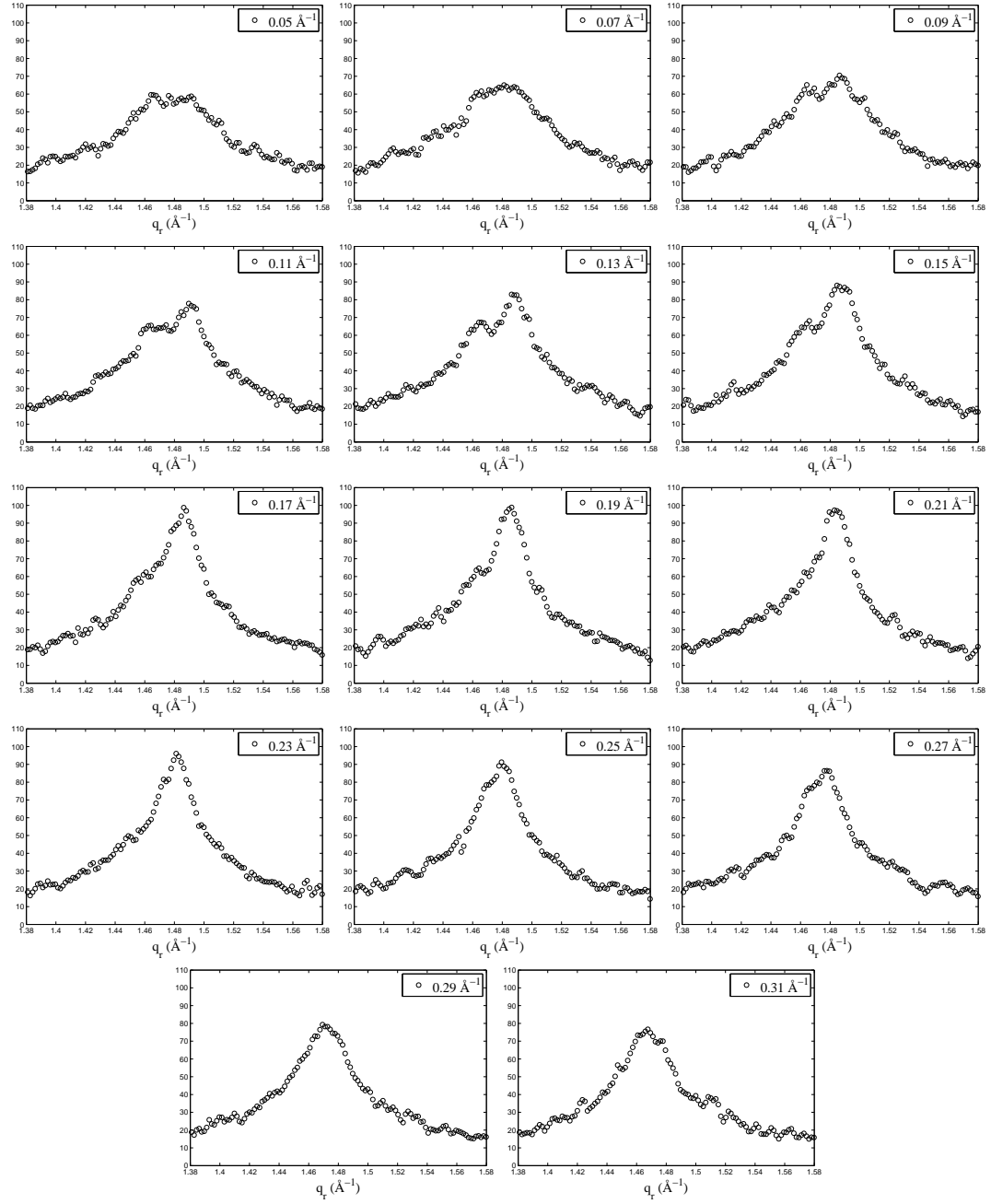


Figure 4.25:  $q_r$  swaths, each averaged over  $0.02 \text{ \AA}^{-1}$ . The center  $q_z$  value of a swath is shown in the figure legends.

## 4.6 Discussion

Comparison with previous unoriented/oriented stuff.

## 4.7 Conclusion

Future possible experiments include the high resolution transmission experiment, where both geometric broadening and energy dispersion are minimized. The expected resolution is the width of the X-ray beam, which is about 3 pixels. This experiment doubles the best resolution achieved in this work. Another slightly different high resolution experiment is to use silicon crystal analyzer downstream of the sample, which completely remove geometric broadening. The downside of this type of high resolution experiment is that only one point in  $q$ -space is probed at any given exposure, so to get a full 2D map of wide angle scattering is time consuming.



# Appendices

# Appendix A

## Tat

### A.1 Analysis of Fixed Angle Data using NFIT

In this section, I propose a slightly new method to analyze the diffuse scattering data. This method may allow us to measure the X-ray form factor at lower  $q_z$  than we have traditionally measured.

#### A.1.1 Theory

#### A.1.2 Results

### A.2 Proper Incorporation of Mosaic Spread to NFIT analysis

First we describe the theory of mosaic spread for diffuse scattering. Next we discuss some simplification. Third, we discuss the program. Fourth, we show the results.

#### A.2.1 Mosaic Spread: Calculation

(Some things are messed up.) In this section, an analytical framework for a measurement of mosaic spread will be developed. Let us imagine that a sample is made up of many small domains that are tilted from the direction perpendicular to the substrate normal by some amount. A "perfect" domain is a domain that is parallel to the substrate plane. Then, we can consider a probability distribution function,

$P(\alpha)$ , representing a probability of finding a domain with tilt  $\alpha$ , which is the angle between the substrate normal and the tilted domain normal. Here, we have assumed the rotational symmetry about the substrate normal, so that the distribution does not depend on the azimuthal angle,  $\beta$ . The normalization condition on the probability distribution is

$$1 = \int_0^{2\pi} d\beta \int_0^{\frac{\pi}{2}} d\alpha \sin \alpha P(\alpha). \quad (\text{A.1})$$

The object of this section is to derive the x-ray scattering structure factor including the probability distribution. The coordinate system employed here is such that x, y, and z-axes of the zero tilt domain, that is, a domain parallel to the substrate, coincide with the lab x, y, and z-axes

First, we want to calculate the structure factor for a domain tilted by  $\alpha$  and  $\beta$ , expressed in the lab coordinates (Need a figure). For this, we need to express  $\mathbf{q}$  in terms of . We imagine rotating the coordinates about the y-axis first, and then about the z-axis. In other words, we apply the appropriate rotation matrices to , y, and z-axes. The rotation matrix for rotating a vector about y-axis is given by

$$\begin{pmatrix} \cos \alpha & 0 & -\sin \alpha \\ 0 & 1 & 0 \\ \sin \alpha & 0 & \cos \alpha \end{pmatrix} \quad (\text{A.2})$$

and for rotating about z-axis

$$\begin{pmatrix} \cos \beta & \sin \beta & 0 \\ -\sin \beta & \cos \beta & 0 \\ 0 & 0 & 1 \end{pmatrix} \quad (\text{A.3})$$

Then, what we want is

$$\hat{\mathbf{x}}' = \begin{pmatrix} \cos \beta & \sin \beta & 0 \\ -\sin \beta & \cos \beta & 0 \\ 0 & 0 & 1 \end{pmatrix} \begin{pmatrix} \cos \alpha & 0 & -\sin \alpha \\ 0 & 1 & 0 \\ \sin \alpha & 0 & \cos \alpha \end{pmatrix} \begin{pmatrix} 1 \\ 0 \\ 0 \end{pmatrix} = \begin{pmatrix} \cos \alpha \cos \beta \\ \cos \alpha \sin \beta \\ -\sin \alpha \end{pmatrix} \quad (\text{A.4})$$

$$\hat{\mathbf{y}}' = \begin{pmatrix} \cos \beta & \sin \beta & 0 \\ -\sin \beta & \cos \beta & 0 \\ 0 & 0 & 1 \end{pmatrix} \begin{pmatrix} \cos \alpha & 0 & -\sin \alpha \\ 0 & 1 & 0 \\ \sin \alpha & 0 & \cos \alpha \end{pmatrix} \begin{pmatrix} 0 \\ 1 \\ 0 \end{pmatrix} = \begin{pmatrix} -\sin \beta \\ \cos \beta \\ 0 \end{pmatrix} \quad (\text{A.5})$$

$$\hat{\mathbf{z}}' = \begin{pmatrix} \cos \beta & \sin \beta & 0 \\ -\sin \beta & \cos \beta & 0 \\ 0 & 0 & 1 \end{pmatrix} \begin{pmatrix} \cos \alpha & 0 & -\sin \alpha \\ 0 & 1 & 0 \\ \sin \alpha & 0 & \cos \alpha \end{pmatrix} \begin{pmatrix} 0 \\ 0 \\ 1 \end{pmatrix} = \begin{pmatrix} \sin \alpha \cos \beta \\ \sin \alpha \sin \beta \\ \cos \alpha \end{pmatrix} \quad (\text{A.6})$$

Then, the components of  $\mathbf{q}$  represented in the rotated coordinates, denoted by  $\mathbf{q}'$ , are the projection of  $\mathbf{q}$  on  $x'$ ,  $y'$ , and  $z'$ -axes, that is,

$$q'_x = \mathbf{q} \cdot \hat{\mathbf{x}}' = q_x \cos \alpha \cos \beta + q_y \cos \alpha \sin \beta - q_z \sin \alpha \quad (\text{A.7})$$

$$q'_y = \mathbf{q} \cdot \hat{\mathbf{y}}' = -q_x \sin \beta + q_y \cos \beta \quad (\text{A.8})$$

$$q'_z = \mathbf{q} \cdot \hat{\mathbf{z}}' = q_x \sin \alpha \cos \beta + q_y \sin \alpha \sin \beta + q_z \cos \alpha \quad (\text{A.9})$$

The transformation rule we are looking for is

$$\cos \theta' = \frac{q'_z}{q} = \sin \theta \sin \alpha \cos(\phi - \beta) + \cos \theta \cos \alpha \quad (\text{A.10})$$

and

$$\tan \phi' = \frac{q'_y}{q'_x} = \frac{\sin \theta \sin(\phi - \beta)}{\sin \theta \cos \alpha \cos(\phi - \beta) - \cos \theta \sin \alpha} \quad (\text{A.11})$$

The structure factor of the tilted domain in the lab coordinates is simply given by  $S(\mathbf{q}') = S(q, \theta', \phi')$ . Summing over all the domains, we get for the total structure factor

$$S_M(q, \theta, \phi) = \int_0^{2\pi} d\beta \int_0^{\frac{\pi}{2}} d\alpha \sin \alpha S(q, \theta', \phi') P(\alpha) \quad (\text{A.12})$$

with Eq. (A.10) and Eq. (A.11).

For  $\theta = 0$ ,  $\theta' = \alpha$  and  $\phi' = 0$  or  $\pi$ , so we have

$$S_M(q, 0) \sim \int_0^{\frac{\pi}{2}} d\alpha \sin \alpha S(q, \alpha, 0) P(\alpha) + \int_0^{\frac{\pi}{2}} d\alpha \sin \alpha S(q, \alpha, \pi) P(\alpha) \quad (\text{A.13})$$

$$= \int_{-\frac{\pi}{2}}^{\frac{\pi}{2}} d\alpha \sin \alpha S(q, \alpha) P(\alpha) \quad (\text{A.14})$$

if we understand  $S(q, \alpha)$  to be the structure factor on the  $(q_r, q_z)$  plane. This shows that  $S_M(q, 0)$  is equal to the convolution of the distribution function and the original structure factor. In general, however,  $S_M(q, \theta)$  is not a convolution of the distribution function and the structure factor.

Given Eqs. (A.10), (A.11), and (A.12), we want to show that mosaic spread acts

as one dimensional convolution in the x-ray structure factor:

$$S_M(q, \theta) = \int_{-\pi}^{\pi} d\alpha S(q, \theta - \alpha) P(\alpha) \quad (\text{A.15})$$

The structure factor representing Bragg peaks in the spherical coordinates are written as

$$S(q, \theta, \phi) \sim \frac{\delta(q - \frac{2\pi h}{D})}{q^2} \delta(\cos \theta - 1) \delta(\phi) \quad (\text{A.16})$$

where  $\delta(x)$  is the Dirac delta function. Plugging Eq. (A.16) in Eq. (A.12), we obtain  $\phi - \beta = 0$ . Using this condition, we get

$$S_M(q, \theta) \sim \frac{\delta(q - \frac{2\pi h}{D})}{q^2} P(\theta) \sin \theta, \quad (\text{A.17})$$

which shows that we can directly measure the probability distribution experimentally by looking at the intensity along  $q = 2\pi h/D$ . In the next section, we will discuss the relevant experimental techniques.

## A.2.2 Mosaic Spread: Experiment

(Under construction) In this section, we discuss experimental procedures to probe appropriate  $q$ -space to measure the mosaic distribution,  $P(\alpha)$ . In our setup, the angle of incidence between the beam and substrate, denoted by  $\omega$ , can be varied. A conventional method to measure mosaicity distribution is a rocking scan, where one measures the integrated intensity of a given Bragg peak as a function of  $\omega$  with a fixed detector position. In a non-conventional method called ring analysis, one measures the intensity as a function of  $\eta$  on a two dimensional detector. First, we want to show that the two methods mentioned above in fact measure the mosaicity distribution and therefore are equivalent to each other.

Let  $\omega$  be the angle of incidence,  $2\theta$  be the total scattering angle,  $p_x$  be the pixel number in the horizontal direction,  $p_z$  be the pixel number in the vertical direction,  $\eta$  be the angle measured from the  $p_z$ -axis on the detector.  $\Delta p$  is 0.07113 mm/pixel.  $q_x = \mathbf{q} \cdot \hat{\mathbf{x}}$ ,  $q_y = \mathbf{q} \cdot \hat{\mathbf{y}}$ , and  $q_z = \mathbf{q} \cdot \hat{\mathbf{z}}$ , where  $\hat{\mathbf{x}}$ ,  $\hat{\mathbf{y}}$ , and  $\hat{\mathbf{z}}$  are all defined on the sample space. This means that  $\hat{\mathbf{y}}$  and  $\hat{\mathbf{z}}$  both rotate as  $\omega$  is varied while  $\hat{\mathbf{x}}$  is always perpendicular to the beam. What we need is a set of transformation rules for going from the detector space (pixels) to the sample  $q$ -space. With them, we would know

how to trace out a line on the detector in order to measure the mosaicity distribution.

In terms of the coordinates defined in section 4.3.2, in the rocking scan,  $\phi = \pi/2$  and  $q = 2\pi h/D$  while  $\omega$  is varied about  $\theta_B$ , where  $\theta_B$  is the Bragg angle for a Bragg peak that is focused on. Using  $q = 4\pi \sin \theta / \lambda$ , we recover the Bragg condition,  $2D \sin \theta = h\lambda$ . Plugging  $\phi = \pi/2$  in Eq. (??), (??), and (??), and taking  $\theta = \theta_B$ ,

### **A.2.3 Results**

## **A.3 Domain Size Distribution: Gaussian and Exponential**

## **A.4 Hard Wall Constraints in SDP**

## **A.5 Some More Details of Tat Stuff**

# Appendix B

## Ripple Phase

### B.1 Derivation of the contour part of the form factor

In this section, we derive  $F_C$ . The ripple profile,  $u(x)$  is given by

$$u(x) = \begin{cases} -\frac{A}{\lambda_r - x_0} \left(x + \frac{\lambda_r}{2}\right) & \text{for } -\frac{\lambda_r}{2} \leq x < -\frac{x_0}{2} \\ \frac{A}{x_0} x & \text{for } -\frac{x_0}{2} \leq x \leq \frac{x_0}{2} \\ -\frac{A}{\lambda_r - x_0} \left(x - \frac{\lambda_r}{2}\right) & \text{for } \frac{x_0}{2} < x \leq \frac{\lambda_r}{2} \end{cases} \quad (\text{B.1})$$

The contour part of the form factor is the Fourier transform of the contour function,  $C(x, z)$ ,

$$F_C(\mathbf{q}) = \frac{1}{\lambda_r} \int_{-\frac{\lambda_r}{2}}^{\frac{\lambda_r}{2}} dx \int_{-\frac{D}{2}}^{\frac{D}{2}} dz C(x, z) e^{iq_z z} e^{iq_x x}$$

As discussed in section X, the modulated models allow the electron density to modulate along the ripple direction,  $x$ . This means

$$C(x, z) = \begin{cases} f_1 \delta[z - u(x)] & \text{for } -\frac{\lambda_r}{2} \leq x < -\frac{x_0}{2} \\ \delta[z - u(x)] & \text{for } -\frac{x_0}{2} < x < \frac{x_0}{2} \\ f_1 \delta[z - u(x)] & \text{for } \frac{x_0}{2} \leq x < \frac{\lambda_r}{2} \end{cases} + f_2 \delta\left(x + \frac{x_0}{2}\right) \delta\left(z + \frac{A}{2}\right) + f_2 \delta\left(x - \frac{x_0}{2}\right) \delta\left(z - \frac{A}{2}\right). \quad (\text{B.2})$$

The contribution from the minor arm is

$$\begin{aligned}
& \frac{1}{\lambda_r} \int_{-\frac{\lambda_r}{2}}^{-\frac{x_0}{2}} dx e^{iq_x x} e^{iq_z u(x)} + \int_{\frac{x_0}{2}}^{\frac{\lambda_r}{2}} dx e^{iq_x x} e^{iq_z u(x)} \\
&= \frac{1}{\lambda_r} \int_{\frac{x_0}{2}}^{\frac{\lambda_r}{2}} dx e^{-i[q_x x - q_z \frac{A}{\lambda_r - x_0}(x - \frac{\lambda_r}{2})]} + \int_{\frac{x_0}{2}}^{\frac{\lambda_r}{2}} dx e^{i[q_x x - q_z \frac{A}{\lambda_r - x_0}(x - \frac{\lambda_r}{2})]} \\
&= \frac{2}{\lambda_r} \int_{\frac{x_0}{2}}^{\frac{\lambda_r}{2}} \cos \left[ \left( q_x - q_z \frac{A}{\lambda_r - x_0} \right) x + q_z \frac{A}{\lambda_r - x_0} \frac{\lambda_r}{2} \right] dx
\end{aligned} \tag{B.3}$$

Using a trigonometric identity,

$$\sin u - \sin v = 2 \cos[(u + v)/2] \sin[(u - v)/2],$$

and defining

$$\omega(\mathbf{q}) = \frac{1}{2} (q_x x_0 + q_z A), \tag{B.4}$$

we further simplify Eq. (B.3),

$$\begin{aligned}
&= \frac{2}{\lambda_r} \frac{\lambda_r - x_0}{\frac{1}{2} q_x \lambda_r - \omega} \cos \left[ \frac{1}{2} \left( \frac{1}{2} q_x \lambda_r + \omega \right) \right] \sin \left[ \frac{1}{2} \left( \frac{1}{2} q_x \lambda_r - \omega \right) \right] \\
&= \frac{1}{\lambda_r} \frac{\lambda_r - x_0}{\frac{1}{2} q_x \lambda_r - \omega} \cos \left[ \frac{1}{2} \left( \frac{1}{2} q_x \lambda_r + \omega \right) \right] \frac{\sin \left( \frac{1}{2} q_x \lambda_r - \omega \right)}{\cos \left[ \frac{1}{2} \left( \frac{1}{2} q_x \lambda_r - \omega \right) \right]} \\
&= \frac{\lambda_r - x_0}{\lambda_r} \frac{\cos \left[ \frac{1}{2} \left( \frac{1}{2} q_x \lambda_r + \omega \right) \right] \sin \left( \frac{1}{2} q_x \lambda_r - \omega \right)}{\cos \left[ \frac{1}{2} \left( \frac{1}{2} q_x \lambda_r - \omega \right) \right] \frac{1}{2} q_x \lambda_r - \omega}.
\end{aligned} \tag{B.5}$$

Similarly, we calculate the contribution from the major arm,

$$\begin{aligned}
\frac{1}{\lambda_r} \int_{-\frac{x_0}{2}}^{\frac{x_0}{2}} dx e^{i \left( \frac{q_z A}{x_0} + q_x \right) x} &= \frac{2}{\lambda_r} \int_0^{\frac{x_0}{2}} dx \cos \left( \frac{q_z A}{x_0} + q_x \right) x \\
&= \frac{x_0}{\lambda_r} \frac{\sin \omega}{\omega}
\end{aligned} \tag{B.6}$$

The contribution from the kink region is

$$\begin{aligned}
& \frac{1}{\lambda_r} \iint dx dz \left[ \delta \left( x + \frac{x_0}{2} \right) \delta \left( z + \frac{A}{2} \right) + \delta \left( x - \frac{x_0}{2} \right) \delta \left( z - \frac{A}{2} \right) \right] e^{iq_x x} e^{iq_z z} \\
&= \frac{2}{\lambda_r} \cos \omega.
\end{aligned} \tag{B.7}$$



Therefore,

$$F_C(\mathbf{q}) = \frac{x_0}{\lambda_r} \frac{\sin \omega}{\omega} + f_1 \frac{\lambda_r - x_0}{\lambda_r} \frac{\cos \left[ \frac{1}{2} \left( \frac{1}{2} q_x \lambda_r + \omega \right) \right]}{\cos \left[ \frac{1}{2} \left( \frac{1}{2} q_x \lambda_r - \omega \right) \right]} \frac{\sin \left( \frac{1}{2} q_x \lambda_r - \omega \right)}{\frac{1}{2} q_x \lambda_r - \omega} + \frac{2f_2}{\lambda_r} \cos \omega \quad (\text{B.8})$$

## B.2 Rotation of a Two-Dimensional Function

Let us consider rotating a function,  $f(x, z)$  in two dimensions by an angle,  $\psi$ , in the counterclockwise direction (see Fig. X). This is easily achieved by rotating the coordinate system by  $\psi$  in the clockwise direction. Let rotated coordinates be  $x'$  and  $z'$ . A point in the original coordinates,  $(x, z)$ , is written as  $(x', z')$  in the new coordinates. More specifically, the point  $\mathbf{P}$  is written as  $\mathbf{P} = x\hat{\mathbf{x}} + z\hat{\mathbf{z}} = x'\hat{\mathbf{x}}' + z'\hat{\mathbf{z}}'$ .  $\hat{\mathbf{x}}$  and  $\hat{\mathbf{z}}$  in the  $x'z'$  coordinate system are written as

$$\hat{\mathbf{x}} = \cos \psi \hat{\mathbf{x}}' + \sin \psi \hat{\mathbf{z}}' \quad (\text{B.9})$$

$$\hat{\mathbf{z}} = -\sin \psi \hat{\mathbf{x}}' + \cos \psi \hat{\mathbf{z}}'. \quad (\text{B.10})$$

Plugging these in  $\mathbf{P} = x\hat{\mathbf{x}} + z\hat{\mathbf{z}}$  leads to

$$x' = x \cos \psi - z \sin \psi \quad (\text{B.11})$$

$$z' = z \cos \psi + x \sin \psi, \quad (\text{B.12})$$

the inverse of which is

$$x = x' \cos \psi + z' \sin \psi \quad (\text{B.13})$$

$$z = -x' \sin \psi + z' \cos \psi. \quad (\text{B.14})$$

Using the latter equations,  $f(x, z)$  can be expressed in terms of  $x'$  and  $z'$ . The resulting function  $f(x', z')$  is the rotated version of  $f(x, z)$ .

As an example, let us consider a Dirac delta function located at  $(x, z) = (0, Z_H)$ ,

that is,  $f(x, z) = \delta(x)\delta(z - Z_{\text{H}})$ . After the rotation by  $\psi$ , it becomes

$$\begin{aligned}
f(x, z) &\rightarrow \delta(x \cos \psi + z \sin \psi) \delta(-x \sin \psi + z \cos \psi - Z_{\text{H}}) \\
&= \frac{\delta(x + z \tan \psi)}{|\cos \psi|} \frac{\delta(-x \sin \psi \cos \psi + z \cos^2 \psi - Z_{\text{H}} \cos \psi)}{1/|\cos \psi|} \\
&= \delta(x + z \tan \psi) \delta(z \tan \psi \sin \psi \cos \psi + z \cos^2 \psi - Z_{\text{H}} \cos \psi) \\
&= \delta(x + z \tan \psi) \delta(z - Z_{\text{H}} \cos \psi),
\end{aligned}$$

which is a part of the expression for  $T_\psi(x, z)$  in the simple delta function model.

### B.3 Derivation of the transbilayer part of the form factor in the 2G hybrid model

In this section, we derive the trasbilayer part of the form factor calculated from the 2G hybrid model discussed in section X. Defining  $z' = -x \sin \psi + z \cos \psi$ , the Fourier transform of a Gaussian function along the line tilted from  $z$ -axis by  $\psi$  is

$$\begin{aligned}
&\iint dz dx \rho_{\text{Hi}} \exp\left\{-\frac{(z' - Z_{\text{Hi}})^2}{2\sigma_{\text{Hi}}^2}\right\} \delta(x \cos \psi + z \sin \psi) e^{iq_x x} e^{iq_z z} \\
&= \frac{1}{\cos \psi} \int_{-\frac{D}{2}}^{\frac{D}{2}} dz \rho_{\text{Hi}} \exp\left\{-\frac{(z - Z_{\text{Hi}} \cos \psi)^2}{2\sigma_{\text{Hi}}^2 \cos^2 \psi} + i(q_z - q_x \tan \psi)z\right\} \\
&\approx \rho_{\text{Hi}} \sqrt{2\pi} \sigma_{\text{Hi}} \exp\left\{i\alpha Z_{\text{Hi}} - \frac{1}{2}\alpha^2 \sigma_{\text{Hi}}^2\right\}
\end{aligned} \tag{B.15}$$

with  $\alpha = q_z \cos \psi - q_x \sin \psi$ . Using Eq. (B.15) and adding the other side of the bilayer and the terminal methyl term, we get

$$\begin{aligned}
F_{\text{G}} &= \sqrt{2\pi} \left[ -\rho_{\text{M}} \sigma_{\text{M}} \exp\left\{-\frac{1}{2}\alpha^2 \sigma_{\text{M}}^2\right\} \right. \\
&\quad \left. + \sum_{i=1}^{1 \text{ or } 2} 2\rho_{\text{Hi}} \sigma_{\text{Hi}} \cos(\alpha Z_{\text{Hi}}) \exp\left\{-\frac{1}{2}\alpha^2 \sigma_{\text{Hi}}^2\right\} \right]. \tag{B.16}
\end{aligned}$$

The strip part of the model in the minus fluid convention is

$$\rho_S(z) = \begin{cases} -\Delta\rho & \text{for } 0 \leq z < Z_{\text{CH}_2} \cos \psi, \\ 0 & \text{for } Z_W \cos \psi \leq z \leq D/2, \end{cases} \quad (\text{B.17})$$

where  $\Delta\rho = \rho_W - \rho_{\text{CH}_2}$ . Then, the corresponding Fourier transform is

$$\begin{aligned} F_S &= \iint dz dx e^{iq_x x} e^{iq_z z} \rho_S(z) \delta(x \cos \psi + z \sin \psi) \\ &= \frac{2}{\cos \psi} \int_0^{Z_{\text{CH}_2} \cos \psi} dz \cos\left(\frac{\alpha}{\cos \psi} z\right) (-\Delta\rho) \\ &= -2\Delta\rho \frac{\sin(\alpha Z_{\text{CH}_2})}{\alpha}. \end{aligned} \quad (\text{B.18})$$

The bridging part of the model in the minus fluid convention is

$$\rho_B(x, z) = \frac{\Delta\rho}{2} \cos\left[\frac{-\pi}{\Delta Z_H}(z' - Z_W)\right] - \frac{\Delta\rho}{2} \quad (\text{B.19})$$

for  $Z_{\text{CH}_2} \cos \psi < z < Z_W \cos \psi$ , and 0 otherwise. Here,  $\Delta Z_H = Z_W - Z_{\text{CH}_2}$ . Then, for the strip part of the form factor, we have

$$\begin{aligned} F_B &= \iint dz dx e^{iq_x x} e^{iq_z z} \delta(x \cos \psi + z \sin \psi) \rho_B(x, z) \\ &= \frac{\Delta\rho}{\cos \psi} \int_{Z_{\text{CH}_2} \cos \psi}^{Z_W \cos \psi} dz \cos\left(\alpha \frac{z}{\cos \psi}\right) \left\{ \cos\left[-\frac{\pi}{\Delta Z_H} \left(\frac{z}{\cos \psi} - Z_W\right)\right] - 1 \right\} \\ &= \Delta\rho \left\{ \frac{\Delta Z_H \sin\left[\frac{\pi(-u+Z_W)}{\Delta Z_H} + \alpha u\right]}{-2\pi + 2\alpha \Delta Z_H} + \frac{\Delta Z_H \sin\left[\frac{\pi(u-Z_W)}{\Delta Z_H} + \alpha u\right]}{2\pi + 2\alpha \Delta Z_H} - \frac{\sin(\alpha u)}{\alpha} \right\} \Bigg|_{Z_{\text{CH}_2}}^{Z_W} \\ &= -\frac{\Delta\rho}{\alpha} [\sin(\alpha Z_W) - \sin(\alpha Z_{\text{CH}_2})] \\ &\quad + \frac{\Delta\rho}{2} \left( \frac{1}{\alpha + \frac{\pi}{\Delta Z_H}} + \frac{1}{\alpha - \frac{\pi}{\Delta Z_H}} \right) [\sin(\alpha Z_W) + \sin(\alpha Z_{\text{CH}_2})]. \end{aligned} \quad (\text{B.20})$$

Because our X-ray scattering intensity was measured in a relative scale, an overall scaling factor was necessary for a non linear least square fitting procedure. This means that  $\Delta\rho$  can be absorbed in the scaling factor. Doing so means that the values of  $\rho_{\text{Hi}}$  and  $\rho_{\text{M}}$  resulting from a fitting procedure are relative to  $\Delta\rho$ . One way to have these parameters in the absolute scale is to integrate the bilayer electron density over

the lipid volume and equate the result to the total number of electrons in the lipid, which can easily be calculated from the chemical formula. For the ripple phase study in this thesis, the absolute values of the electron density were not of importance, so the discussion was omitted in the main text.

## B.4 Correction due to refractive index

$q_z$  needs be corrected for index of refraction. This section is practically the same as an appendix in Yufeng Liu's thesis. I include this section for mere convenience.

Let  $\theta'$  and  $\lambda'$  be the true scattering angle and wavelength within the sample. The wavelength by an energy analyzer,  $\lambda$ , and the scattering angle calculated from a position on a CCD detector,  $\theta$  are apparent. The correction is not necessary in the horizontal direction. The Snell's law in Fig. X gives

$$n \cos \theta = n' \cos \theta' \quad (\text{B.21})$$

$$n\lambda = n'\lambda'. \quad (\text{B.22})$$

For low angle X-ray scattering, the momentum transfer along  $z$  direction is

$$q_z = \frac{4\pi \sin \theta'}{\lambda'} \quad (\text{B.23})$$

$$= \frac{4\pi n'}{n\lambda} \sin \theta' \quad (\text{B.24})$$

$$= \frac{4\pi n'}{n\lambda} \sqrt{1 - \cos^2 \theta'} \quad (\text{B.25})$$

$$= \frac{4\pi n'}{n\lambda} \sqrt{1 - \left(\frac{n}{n'} \cos \theta\right)^2}. \quad (\text{B.26})$$

The apparent scattering angle,  $\theta$ , is directly related to the vertical pixel position,  $p_z$ , by

$$\theta = \frac{1}{2} \tan^{-1} \left( \frac{p_z}{S} \right), \quad (\text{B.27})$$

where  $S$  is the sample-to-detector distance. The typical units of  $S$  and  $p_z$  are in mm. In our experimental setup,  $n = 1$  and  $n' = 0.9999978$  for lipids at  $\lambda = 1.18 \text{ \AA}$ .

# Bibliography

- [1] Daniel C. Wack and Watt W. Webb. Synchrotron x-ray study of the modulated lamellar phase  $p\beta'$  in the lecithin-water system. *Phys. Rev. A*, 40:2712–2730, Sep 1989.
- [2] Norbert Kuerka, John F. Nagle, Jonathan N. Sachs, Scott E. Feller, Jeremy Pencer, Andrew Jackson, and John Katsaras. Lipid bilayer structure determined by the simultaneous analysis of neutron and x-ray scattering data. *Biophysical Journal*, 95(5):2356 – 2367, 2008.
- [3] Stephanie Tristram-Nagle, Yufeng Liu, Justin Legleiter, and John F. Nagle. Structure of gel phase DMPC determined by x-ray diffraction. *Biophysical Journal*, 83(6):3324 – 3335, 2002.
- [4] Anthony R. Braun, Jonathan N. Sachs, and John F. Nagle. Comparing simulations of lipid bilayers to scattering data: The gromos 43a1-s3 force field. *The Journal of Physical Chemistry B*, 117(17):5065–5072, 2013.
- [5] <http://seal.web.cern.ch/seal/documents/minuit/mnusersguide.pdf>.
- [6] <http://lcgapp.cern.ch/project/cls/work-packages/mathlibs/minuit/index.html>.
- [7] Berk Hess, Carsten Kutzner, David van der Spoel, and Erik Lindahl. Gromacs 4: Algorithms for highly efficient, load-balanced, and scalable molecular simulation. *Journal of Chemical Theory and Computation*, 4(3):435–447, 2008.
- [8] Joakim P. M. Jmbeck and Alexander P. Lyubartsev. Derivation and systematic validation of a refined all-atom force field for phosphatidylcholine lipids. *The Journal of Physical Chemistry B*, 116(10):3164–3179, 2012.

- [9] Joakim P. M. Jmbeck and Alexander P. Lyubartsev. An extension and further validation of an all-atomistic force field for biological membranes. *Journal of Chemical Theory and Computation*, 8(8):2938–2948, 2012.
- [10] Viktor Hornak, Robert Abel, Asim Okur, Bentley Strockbine, Adrian Roitberg, and Carlos Simmerling. Comparison of multiple amber force fields and development of improved protein backbone parameters. *Proteins: Structure, Function, and Bioinformatics*, 65(3):712–725, 2006.
- [11] Norbert Kuerka, John Katsaras, and JohnF. Nagle. Comparing membrane simulations to scattering experiments: Introducing the simtoexp software. *Journal of Membrane Biology*, 235(1):43–50, 2010.
- [12] A. Tardieu, Vittorio Luzzati, and F.C. Reman. Structure and polymorphism of the hydrocarbon chains of lipids: A study of lecithin-water phases. *Journal of Molecular Biology*, 75(4):711 – 733, 1973.
- [13] JA Zasadzinski, J Schneir, J Gurley, V Elings, and PK Hansma. Scanning tunneling microscopy of freeze-fracture replicas of biomembranes. *Science*, 239(4843):1013–1015, 1988.
- [14] W J Sun, S Tristram-Nagle, R M Suter, and J F Nagle. Structure of the ripple phase in lecithin bilayers. *Proceedings of the National Academy of Sciences*, 93(14):7008–7012, 1996.
- [15] M. P. Hentschel and F. Rustichelli. Structure of the ripple phase  $\pi$  in hydrated phosphatidylcholine multimembranes. *Phys. Rev. Lett.*, 66:903–906, Feb 1991.
- [16] Alex H. de Vries, Serge Yefimov, Alan E. Mark, and Siewert J. Marrink. Molecular structure of the lecithin ripple phase. *Proceedings of the National Academy of Sciences of the United States of America*, 102(15):5392–5396, 2005.
- [17] [http://henke.lbl.gov/optical\\_constants](http://henke.lbl.gov/optical_constants).

- [18] M.C. Wiener, R.M. Suter, and J.F. Nagle. Structure of the fully hydrated gel phase of dipalmitoylphosphatidylcholine. *Biophysical Journal*, 55(2):315 – 325, 1989.